



ARL-TR-8985 • JULY 2020



Understanding the Nanoscale Inhomogeneity in Commercial Detonation Nanodiamonds via Advanced Material Characterization

by Chi-Chin Wu, Scott D Walck, Frederick L Beyer, Jennifer L
Gottfried, Kelsea K Miller, and Rose A Pesce-Rodriguez

Approved for public release; distribution is unlimited.

NOTICES

Disclaimers

The findings in this report are not to be construed as an official Department of the Army position unless so designated by other authorized documents.

Citation of manufacturer's or trade names does not constitute an official endorsement or approval of the use thereof.

Destroy this report when it is no longer needed. Do not return it to the originator.



Understanding the Nanoscale Inhomogeneity in Commercial Detonation Nanodiamonds via Advanced Material Characterization

**Chi-Chin Wu, Frederick L Beyer, Jennifer L Gottfried, and Rose A
Pesce-Rodriguez**

Weapons and Materials Research Directorate, CCDC Army Research Laboratory

Scott D Walck

SURVICE Engineering Company

Kelsea K Miller

Texas Tech University

REPORT DOCUMENTATION PAGE

Form Approved
OMB No. 0704-0188

Public reporting burden for this collection of information is estimated to average 1 hour per response, including the time for reviewing instructions, searching existing data sources, gathering and maintaining the data needed, and completing and reviewing the collection information. Send comments regarding this burden estimate or any other aspect of this collection of information, including suggestions for reducing the burden, to Department of Defense, Washington Headquarters Services, Directorate for Information Operations and Reports (0704-0188), 1215 Jefferson Davis Highway, Suite 1204, Arlington, VA 22202-4302. Respondents should be aware that notwithstanding any other provision of law, no person shall be subject to any penalty for failing to comply with a collection of information if it does not display a currently valid OMB control number.

PLEASE DO NOT RETURN YOUR FORM TO THE ABOVE ADDRESS.

1. REPORT DATE (DD-MM-YYYY) July 2020		2. REPORT TYPE Technical Report		3. DATES COVERED (From - To) 1 January 2018–31 December 2019	
4. TITLE AND SUBTITLE Understanding the Nanoscale Inhomogeneity in Commercial Detonation Nanodiamonds via Advanced Material Characterization				5a. CONTRACT NUMBER	
				5b. GRANT NUMBER	
				5c. PROGRAM ELEMENT NUMBER	
6. AUTHOR(S) Chi-Chin Wu, Scott D Walck, Frederick L Beyer, Jennifer L Gottfried, Kelsea K Miller, and Rose A Pesce-Rodriguez				5d. PROJECT NUMBER	
				5e. TASK NUMBER	
				5f. WORK UNIT NUMBER	
7. PERFORMING ORGANIZATION NAME(S) AND ADDRESS(ES) CCDC Army Research Laboratory ATTN: FCDD-RLW-LB Aberdeen Proving Ground, MD 21005				8. PERFORMING ORGANIZATION REPORT NUMBER ARL-TR-8985	
9. SPONSORING/MONITORING AGENCY NAME(S) AND ADDRESS(ES)				10. SPONSOR/MONITOR'S ACRONYM(S)	
				11. SPONSOR/MONITOR'S REPORT NUMBER(S)	
12. DISTRIBUTION/AVAILABILITY STATEMENT Approved for public release; distribution is unlimited.					
13. SUPPLEMENTARY NOTES ORCID IDs: Chi-Chin Wu, 0000-0002-6036-3271; Frederick L Beyer, 0000-0003-0253-2134; Jennifer L Gottfried, 0000-0002-1282-1928					
14. ABSTRACT Detonation nanodiamonds (DNDs) have been widely used for many applications across different disciplines. As part of an ongoing effort that previously demonstrated variations in the structural stability of different DND samples, this work performed in-depth characterization of commercial DND samples with a special focus on identifying the nanoscale variations in the structural and chemical properties within each sample. High-resolution transmission electron microscopy and electron energy loss spectroscopy in the scanning mode were exploited to elucidate the changes in the structure with diamond-carbon core surrounded by graphitic-carbon layers during electron beam irradiation for DNDs with relatively low impurity content to demonstrate localized variations in structural instability. Although Fourier transform infrared spectroscopy and transmission electron microscopy did not indicate a significant amorphous content, powder X-ray diffraction experiments suggest distinct amorphous character and the presence of organic impurities in the relatively higher-quality diamond samples containing a higher crystallinity and lower metal and organic impurities content. The particle surface properties were also investigated with small-angle X-ray scattering, and the interfacial stability in water suspension was evaluated by zeta potential measurements. Overall, the present work highlights the importance of conducting a thorough characterization to identify the presence of contaminants that may result in unexpected results for applications using what are assumed to be a pure DND with a stable diamond structure.					
15. SUBJECT TERMS detonation nanodiamond, DND, transmission electron microscopy, TEM, scanning transmission electron microscopy, STEM, electron energy loss spectroscopy, EELS, X-ray energy dispersive spectroscopy, XEDS, fast Fourier transform, FFT, powder X-ray diffraction, XRD, small-angle X-ray scattering, SAXS, zeta potential, Z-average diameter					
16. SECURITY CLASSIFICATION OF:			17. LIMITATION OF ABSTRACT UU	18. NUMBER OF PAGES 48	19a. NAME OF RESPONSIBLE PERSON Chi-Chin Wu
a. REPORT Unclassified	b. ABSTRACT Unclassified	c. THIS PAGE Unclassified			19b. TELEPHONE NUMBER (Include area code) 410-306-1905

Contents

List of Figures	iv
List of Tables	v
1. Introduction	1
2. Experiments and Data Analysis	4
3. Results and Discussion	6
3.1 Analysis of Nanoscale Variations in Diamond Crystallinity	6
3.2 New Information on Elemental and Hydrocarbon Impurities	14
3.3 Powder X-ray Diffraction (XRD) Studies	20
3.4 Small-Angle X-ray Scattering (SAXS)	23
3.5 Zeta Potential Measurement and Particle Size Distributions	26
4. Conclusion	30
5. References	34
List of Symbols, Abbreviations, and Acronyms	39
Distribution List	41

List of Figures

Fig. 1	Exposure experiment of the transformation of the diamond structure in the TEM in an area of relative good stability for the DND-4 sample. a) TEM image at the start of imaging, b) FFT of the indicated region of a), and c) radial average of the FFT. d) TEM image after ~10 min, e) FFT of d), and f) radial average of e). g) TEM after 21 min, h) FFT of g), and i) radial average of g). Note the buildup of a broad amorphous peak occurring at $\sim 1.3 \text{ nm}^{-1}$ in f) and i) that is not present in c). 7
Fig. 2	TEM micrographs revealing a faster deterioration of the crystalline diamond core and increasing graphitic onion-like shells in an unstable region of the DND-4 sample using the same current density as the area in Fig. 1: a) at the start of imaging and b) after ~9 min of exposure. The FFT in a) suggests that there may be more amorphous carbon present at the start of the experiment. 8
Fig. 3	TEM micrographs showing faster deterioration of the crystalline diamond core and increasing graphitic onion-like shells of the DND-4 sample with increased current density: a) at the start of imaging and b) after 3 min 9
Fig. 4	STEM EELS of DND-4. a) BF STEM image of DND-4, acquired at a magnification of $2 \text{ M}\times$. The red box indicates an area that would be scanned at the $15 \text{ M}\times$ magnification and suitable for acquiring EELS spectra. b) EELS C-K edge spectrum acquired from a freshly exposed area using a 1-nm beam at $15 \text{ M}\times$. c) A sequence of spectra acquired during scanning using a 1-nm probe at $15 \text{ M}\times$ that shows the increasing π^* peak with a decreasing σ peak. 13
Fig. 5	LIBS spectra of all DND samples with major emission features labeled 15
Fig. 6	Selected regions of the LIBS spectra among the four DND samples showing trace impurities such as Si, Mg, Fe, Ti, Cu, and Al 16
Fig. 7	The TEM-XEDS spectra acquired from different regions in the DND-4 sample along with their corresponding TEM images: a) the background, b) and c) at relatively lower magnifications, and d) at a high magnification 18
Fig. 8	FTIR-microscope spectra of all DND samples 20
Fig. 9	XRD for all the DND samples: a) overall scan from 10° to 95° and b) a zoomed spectrum to show the deconvoluted peaks for a diamond XRD spectrum 22
Fig. 10	SAXS data for each of the four DND samples in this study. Data are shifted vertically for clarity 23
Fig. 11	Results from fitting the SAXS data for DND-1 using the unified model, comprising a Guinier approximation and a Porod's law term 24

Fig. 12	SAXS data for DND-4 and the results of modeling the scattering data using a core-shell form factor. Error bars are shadowed for clarity. ..	26
Fig. 13	Size distributions by scattered light intensity of DND suspensions (0.05–0.1 wt% in deionized water); each color represents the results obtained from one repeat experiment for each sample.	29

List of Tables

Table 1	STEM probe area fraction (probe area/scan area)	11
Table 2	STEM beam exposures	12
Table 3	Results from fitting the SAXS data with the unified model and a core-shell form factor. Here P corresponds to the Porod's exponent in Eq. 1.	25
Table 4	Zeta potential measurement data for all DND samples	27

1. Introduction

Nanodiamonds (NDs), which consist of a diamond core surrounded by a graphitic shell, are known to be promising carbon nanomaterials for many applications such as catalysis, biomedical imaging, drug delivery, metal plating, abrasives coatings, lubricants, and nanocomposites.¹⁻⁶ Because of their unique physical and chemical properties, NDs have been studied at the US Army Combat Capabilities Development Command (CCDC) Army Research Laboratory (ARL) over this past decade with experiments using commercial detonation nanodiamonds (DNDs) and molecular dynamics modeling.^{7,8} In our previous experimental investigation using three commercial samples that were produced by presumably identical conditions from the same vendor,⁹ we found unexpected variations in diamond structures and their relationships to the organic contaminants and metallic impurities that have been often overlooked when exploiting DND for potential advanced applications. In that work, two possible mechanisms were proposed to interpret the observed rapid conversion of crystalline diamond cores to graphitic carbons in the gradually increasing onion-like outer shells under electron beam irradiation during transmission electron microscopy (TEM) experiments and the correlation of this behavior with relatively high concentrations of organic and inorganic contaminants. For NDs, a small π^* peak always exists in the electron energy loss spectroscopy (EELS) spectra. This feature is observed even for samples displaying distinct sp^3 -C diamond character and is ascribed to the outer graphitic shell that results from surface reconstruction.^{7,10} For the DND sample with the highest level of impurities, the conversion of diamond structure from sp^3 -C to sp^2 -C was so profound that the EELS spectra revealed the transformation from diamond to graphite via a broad peak with a growing π^* contribution.

In addition to crystalline diamond and onion shell-like graphitic carbon, amorphous carbon was also observed in the three lots of DNDs, the concentration of which was found to be dependent on the level of hydrocarbon contaminants in the materials.⁹ In response to this finding, a “stacking on diamond” model was proposed to explain the rapid buildup of amorphous carbon on the surface of the diamonds as a result of irradiation of organic contaminants. This effect was only observed for DNDs with a high hydrocarbon impurity content. Literature reports suggest that amorphous carbon content can vary with pressure, temperature, and the overall environment during detonation events used for the production of NDs.¹¹ However, previous studies of commercial DNDs have either rarely mentioned or reported a low content of amorphous carbons.¹⁰ A “consuming diamond” model was proposed as the other possible mechanism in our previous study to explain the observed structural conversion from sp^3 -C diamond to sp^2 -C graphite for commercial DNDs.

This mechanism was supported by a gradual reduction of contrast in the core and the increased number of layered onion shells in the TEM images, accompanied by the emerging π^* peak—a signature graphite peak in EELS.⁹

Regarding possible functional groups in commercial DNDs (either on the surface or in between DND particles), both alkanes and alkenes as large as tricosane ($C_{23}H_{48}$) and nonadecene ($C_{19}H_{38}$) were observed and attributed to either residual wax from the explosive formulations used during detonation or the bags used for storage.⁹ Our chemical analysis results also suggested the presence of anionic surfactants that might have been introduced to DND samples during conventional purification processes. In fact, the presence of different carbon-bonded surface functional groups has been studied widely with various techniques, as described in our previous work.⁹ Using solid-state nuclear magnetic resonance, some of these contaminants can be quantified by calculating the ratios among carbonyl, aldehyde, and aromatic carbons.¹² Using Fourier transform infrared (FTIR) spectroscopy, Ji et al.¹³ suggested quick atmospheric water and hydrocarbon absorption by DNDs even after a thorough cleaning process by acid mixtures. However, the broad asymmetric envelope related to the hydroxyl group was pronounced only for DNDs containing relatively high levels of hydrocarbon contaminants and amorphous carbons. The presence of different types of impurities can facilitate aggregation of DND particles via interaction of organic surface functional groups (e.g., -CH-, -CH₂- and -OH functionalities).

In addition to graphitic carbons on the surface and in between DND particles, metallic impurities are often present inside the crystal lattice of the diamond core.¹⁴ Many metallic impurities, mostly transition metals, were identified by Mitev et al. in 15 commercial DND samples¹⁵ and attributed to synthesis and purification treatments. A technique combining ultrasonic fractioning with ion-exchange resin purification has been developed and claimed to be able to reduce metallic impurities such as iron (Fe) and chromium (Cr).¹⁶ In our previous study,⁹ varying levels of several metallic impurities were identified by laser-induced breakdown spectroscopy (LIBS) in commercial DND samples obtained from the same source. The presence of calcium (Ca), sodium (Na) and potassium (K) was attributed to solvents used in the purification process. In addition, other impurities including Fe, silicon (Si), titanium (Ti), cobalt (Co), and aluminum (Al) were also identified and attributed to residual impurities from the detonation chamber and/or subsequent contamination during sample processing and handling. In that work, element-by-element comparisons of LIBS and TEM X-ray energy-dispersive spectrometry (XEDS) techniques were conducted.

Past efforts to characterize and purify DNDs underscore the importance of further advancements in detection and identification of impurities in commercial DNDs.

Through these advancements, the effects of impurities on structural properties (e.g., crystallinity and stability) can be better understood. Toward this end, Shenderova and McGuire¹⁷ carried out a comprehensive review on ND modification/engineering and the resulting effects on chemical and structural characterization and applications.

The formation of “indestructible aggregates” of DNDs has made morphological characterization very challenging in the past.^{18,19} However, small-angle X-ray scattering (SAXS) has been demonstrated to be a powerful tool for characterizing particle size and size distribution of both dispersed and aggregated nanoparticles (NPs).^{20–22} The simplest approach for characterizing a two-phase system such as particles in a matrix is to use the Guinier approximation, which provides an average radius of gyration (R_g) describing the particulate phase. The particle surface roughness can be analyzed using Porod’s law, which states that intensity of scattered X-rays, $I(q)$, will scale as q^{-4} (where $q = 4\pi \cdot \sin(\theta)/\lambda$, 2θ is the scattering angle, and λ is the X-ray wavelength).²³ Diffuse interfaces, such as the graphitic carbon shell surrounding the diamond core in DNDs, result in negative deviations from Porod’s law.^{24,25} Tomchuk and co-workers used Porod’s analysis in combination with contrast variation on small-angle neutron scattering data to map the transition from the DND diamond core to the graphitic carbon states in the shell, providing a succinct analysis of the change in structure within the DND.²⁶ If the shape of the particulate phase is well defined, the scattering can be better described using a form factor corresponding to the specific shape (sphere, rod, etc.).²³ This approach can be used to calculate the particle size and size distribution accurately, even for mixtures.²² For example, using a core-shell sphere form factor in combination with high-resolution TEM and other techniques, Mykhaylyk and co-workers performed a detailed particle size analysis on DNDs and found an average diamond core diameter of approximately 30 Å with a graphitic shell thickness of roughly 8 Å.²⁷

In our previous work,⁹ we used TEM images to reveal the different morphologies among commercial DND samples. From that study, we also observed that DNDs containing a higher level of impurity content had relatively unstable diamond cores (DND-2). In the present work, we expand our investigations on commercial DNDs to a fourth sample lot produced under nominally identical detonation and purification conditions as the previous three lots. All samples were provided by the same vendor under the same product number.⁹ The fourth sample, DND-4, has been observed to have a much higher level of diamond crystallinity than any of the previous samples. In this work, we demonstrate the locally varying morphological stability of the diamond structure for different regions within the “best” sample, DND-4, by acquiring sequential images of the diamond structure of a specific area

in the TEM field of view. We also monitored the transition of the carbon structure from sp^3 -C diamond to sp^2 -C graphite under electron beam irradiation at normal imaging conditions. In contrast to our previous work where we compared the bulk impurities among the different DND samples, this present work studied the local distribution of impurities within the same relatively “clean” DND-4 sample to emphasize the variations of contaminant types and content levels at the nanoscale in local areas. Samples were examined via XEDS acquisitions at different TEM magnifications. Furthermore, powder X-ray diffraction (XRD) was also exploited to qualitatively compare the relative ratio between diamond and graphitic carbons and identify possible structures corresponding to the peaks containing the organic and elemental impurities. Impurities identified by XRD were also compared with the possible functional groups observed by FTIR. SAXS experiments were conducted, the average particle diameters were derived by the Guinier analysis, and Porod’s analysis provided information on the particle surface roughness for the commercial DNDs. In addition, the extent of particle agglomeration and colloidal instabilities among DND samples dispersed in a water solution was evaluated based on zeta potential measurements, the results of which were correlated to the observed organic surface functional groups. Overall, this work has advanced our understanding of the local variations of structural and chemical properties for common commercial DNDs, both within each sample and among samples of different lots produced by nominally identical experimental conditions. The goal of this work is to raise the awareness of the importance of comprehensive and in-depth material characterization of commercial DND samples prior to using the material for desired applications.

2. Experiments and Data Analysis

Commercial DNDs denoted as DND-1, DND-2, DND-3, and DND-4, having approximately 5-nm average particle sizes based on TEM images, were acquired from Skyspring Nanomaterials, Inc. (Houston, Texas). Here, the DND-1, DND-2, and DND-3 samples were the same as those used in our previous work, with the new sample DND-4 provided to us by the same vendor. The TEM specimens were prepared via a common NP suspension technique using high-purity ethanol (Decon Laboratories, Inc.) as the solvent to disperse the sample powders in solution on the holey carbon-film-coated specimen copper grid (Ted Pella, 300 mesh). The TEM experiments were conducted using a JEOL 2100FX microscope operating at a 200-kV acceleration voltage. The EELS and XEDS spectra were obtained in the scanning transmission electron microscopy (STEM) mode while using high-angle annular dark field (HAADF) imaging. Data were collected using the HAADF4 camera length, with an acquisition range of 45–145 mrad, a convergence angle of

8.3 mrad, an EELS collection angle of 9.7 mrad, and a 0.7-nm probe size that has 375 pA of probe current. Other detailed TEM conditions were similar to the description in our previous work.⁹

The DND samples were prepared for SAXS characterization by sandwiching a small amount (several milligrams) of each dry powder sample between two pieces of pressure-sensitive transparent tape. Two-dimensional SAXS patterns were collected using a SMAX-3000 camera (Rigaku) with a MicroMax-007HFM rotating copper (Cu) anode operated at 40 kV and 30 mA. The resulting characteristic Cu X-rays are then focused and monochromated to the $K\alpha$ doublet with a wavelength (λ) of 1.5418 Å using a confocal max-flux double-focusing optic,²⁸ then shaped using 3-pinhole collimation. Data were collected at two different sample-to-detector distances, 1.5 and 0.5 m, using a 2-D multiwire xenon proportional counter, and then combined to give an effective angular range of $0.008 \leq q \leq 0.7 \text{ \AA}^{-1}$. The instrument calibrations for sample-to-detector distance and beam center were performed using silver behenate ($\text{AgC}_{22}\text{H}_{43}\text{O}_2$). All data corrections and particle size analyses were performed using the software IGOR Pro v7 (Wavemetrics, Inc.), with the software procedures provided by Argonne National Laboratory.^{29,30}

The powder XRD experiments were conducted with a Bruker D2 Phaser diffractometer with a Cu radiation source ($\lambda_{K\alpha 1} = 1.54060 \text{ \AA}$, $\lambda_{K\alpha 2} = 1.54439 \text{ \AA}$, $\lambda_{K\beta} = 1.39222 \text{ \AA}$), 30 kV, 10 mA current X-ray generator, and the 1-D LYNXEYE detector. The scanning conditions were 10° to 100° 2θ scanning range with a 0.04° step size and 8.1 s per step.

The zeta potentials and zeta-average diameters, namely, Z-averages, were obtained using a commercial instrument Zetasizer Nano ZSP (Malvern Inc.) by preparing water suspensions with 0.05–0.1 wt% DND using approximately 2 mL of deionized water as the medium followed by sonication (Sonicate VWR). The 90° detection optical arrangement measures the forward scattering light intensities while the 175° detection optics measure the backscattering light intensities via the noninvasive backscatter (NIBS) technique. The NIBS technique reduces the multiple scattering effects. All measurements were performed at 25°C . The Z-average was analyzed using the cumulants technique.³¹

LIBS was performed using a commercial LIBS system (Ocean Optics, Inc., LIBS-SC), with a Big Sky CFR200 laser (200 mJ, 1064 nm, 9 ns) and a LIBS2500 7-channel charge-coupled device (CCD) spectrometer (200–805 nm, ~ 0.1 -nm resolution, 1.5- μs delay, and 1-ms integration time). Fifteen spectra were averaged for each sample, which were prepared as thin powder residues on double-sided tape.

FTIR spectra of isolated particles were obtained using a Nicolet is50 FTIR spectrometer interfaced to a Nicolet Continuum infrared microscope operating in reflectance mode and equipped with a ReFlacromat 15× objective. For each spectrum, 128 scans were collected at a resolution of 4 cm⁻¹. Spectral searches were performed using the BioRad KnowItAll Informatics System (Analytical Edition) software and database.

3. Results and Discussion

3.1 Analysis of Nanoscale Variations in Diamond Crystallinity

The general structural analysis and comparisons among three samples denoted as DND-1, DND-2, and DND-3 were described in our previous work,⁹ in which we discussed the collective relationship between the DND crystallinity and its diamond core instability to the bulk content of organic contaminants. After performing a general analysis similar to those conducted for the previous three samples on DND-4, we concluded that DND-1 and DND-4 qualitatively possess the best diamond core-shell structures with distinct crystalline diamond cores surrounded by graphitic carbon (onion-like shells) with relatively few impurities. In the present work, we found locally varying regions of instability for the diamond structure of DND samples subjected to electron beam irradiation. Thus, even for those comparatively highly crystalline and pure DND samples (such as DND-1 and DND-4), some regions exhibited extensive structural stability without detectable changes for over 30 min under normal high-resolution TEM imaging conditions, while the diamond crystalline cores in other regions transformed to graphite in as little as several minutes. For example, Fig. 1a is a high-resolution TEM image of the DND-4 sample revealing the high level of crystallinity with a distinct diamond core-shell structure for nearly every particle. The spots in the ring of the fast Fourier transform (FFT) image in Fig. 1b from the indicated red box in Fig. 1a and the peak in the rotational average line profile³² of the FFT image in Fig. 1c correspond to the {111} planes of diamond. Upon exposure to the electron beam, onion-like, graphitic carbon first appears in the vicinity of the outermost surface of the particles with a corresponding faint ring of spots at a radial distance in the FFT corresponding to the {002} planes of graphite. In order to evaluate the stability of the diamond structure during observation in the TEM, we monitored the transformation during observation at high resolution using a current density at the small phosphor screen of approximately 100 pA/cm², which is typically used during image observation and acquisition. This value was first measured using a hole region after the condenser lens was set to a fluence typically used to record high-magnification images. Multiplying this value by the square of the magnification

will give the current density at the sample. The counts from the Orius camera were measured and averaged. In subsequent imaging during the exposure experiment, the average value from the hole regions in the digital images was set to the same value by adjusting the condenser lens.

Figure 1 also shows the transformation sequence during a 21-min exposure using a beam current density at the sample of 1.6×10^{13} pA/cm². After approximately 10 min, Fig. 1d, 1e, and 1f show that the onion-like structure appears in the near surface regions of the particles with small corresponding diffraction from the basal planes of graphite. After approximately 20 min, the isolated particles at the edge of the agglomerated particles have completely transformed with the corresponding better definition of the graphite peaks, as shown in Fig. 1g, 1h, and 1i. In addition, there appears to be a buildup of an amorphous phase that is apparent in the FFTs and the rotational average profiles during beam exposure that was not present at the start of this experiment.

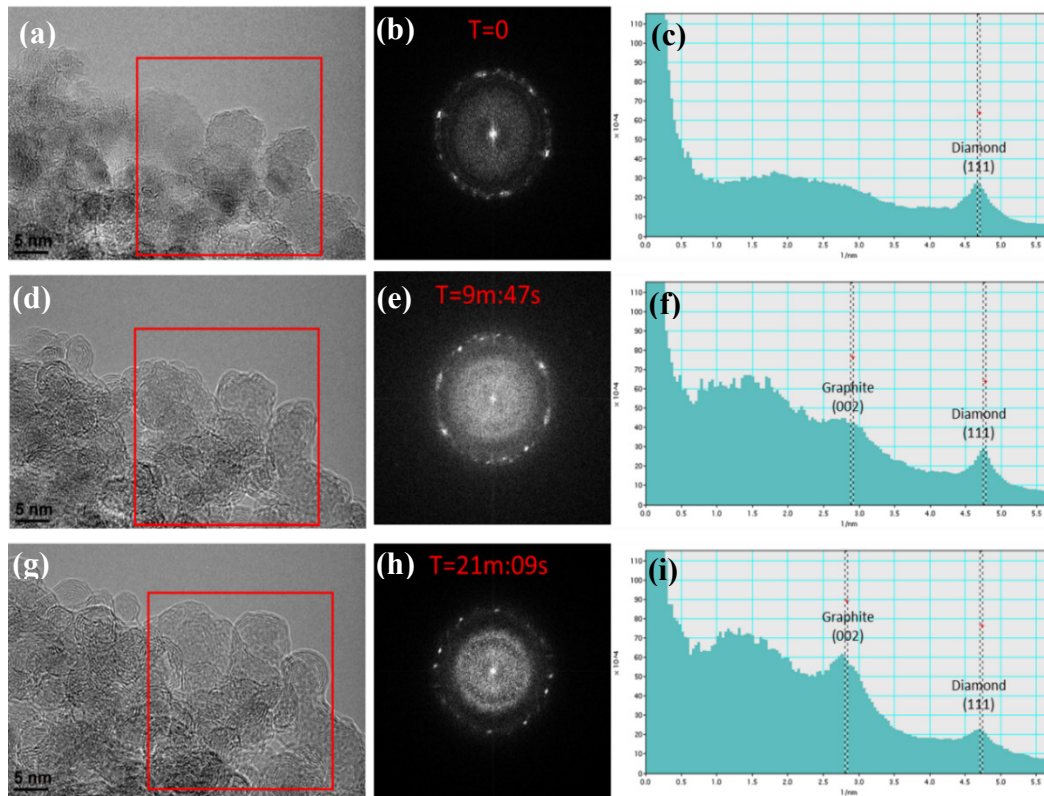


Fig. 1 Exposure experiment of the transformation of the diamond structure in the TEM in an area of relative good stability for the DND-4 sample. a) TEM image at the start of imaging, b) FFT of the indicated region of a), and c) radial average of the FFT. d) TEM image after ~10 min, e) FFT of d), and f) radial average of e). g) TEM after 21 min, h) FFT of g), and i) radial average of g). Note the buildup of a broad amorphous peak occurring at $\sim 1.3 \text{ nm}^{-1}$ in f) and i) that is not present in c).

There are three factors that could affect this transformation rate: beam damage due to radiation, beam heating, and local contaminant concentrations. In reality, it is difficult to separate these factors from each other. Since regions with more agglomerated particles transform more slowly, beam heating may be the predominant factor because they allow the heat to be dissipated more readily.

Figure 2a shows the initial image of another region of the same DND-4 sample by using the same current density that was used in Fig. 1. After 9 min, the NPs have transformed to the onion-like, graphitic structure, as shown in Fig. 2b. This is an example of a region of the same sample that transforms more rapidly. In addition to the crystalline diamond spots in the FFT in Fig. 2a, an amorphous ring, presumably from an amorphous carbon phase, is present. This amorphous ring was not present in the FFT in Fig. 1b. Figure 3 shows the results of an experiment where the beam current density was increased by a factor of 3 compared to Figs. 1 and 2 in an area exhibiting qualitatively similar structural stability as Fig. 1. With a period of 3 min between Fig. 3a and Fig. 3b, the transformation occurs at a much faster rate with the increased current density ($\sim 7\times$) and again the more isolated particles transform faster.

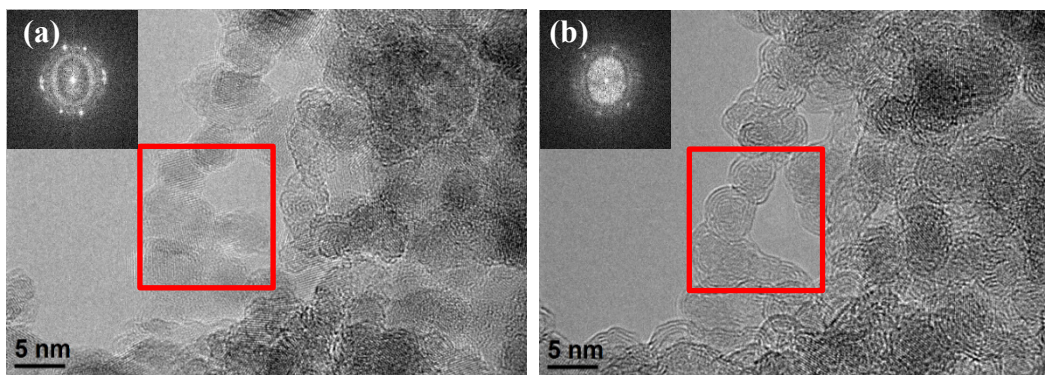


Fig. 2 TEM micrographs revealing a faster deterioration of the crystalline diamond core and increasing graphitic onion-like shells in an unstable region of the DND-4 sample using the same current density as the area in Fig. 1: a) at the start of imaging and b) after ~ 9 min of exposure. The FFT in a) suggests that there may be more amorphous carbon present at the start of the experiment.

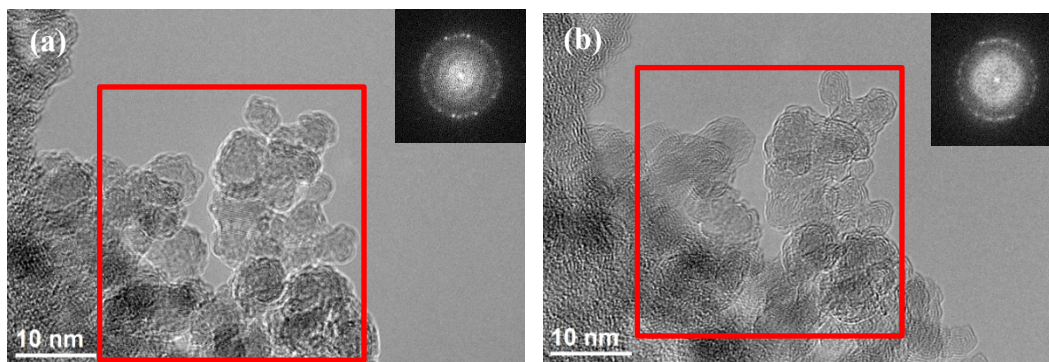


Fig. 3 TEM micrographs showing faster deterioration of the crystalline diamond core and increasing graphitic onion-like shells of the DND-4 sample with increased current density: a) at the start of imaging and b) after 3 min

Although there is no way to separate the combined factors that control the transformation during electron beam exposure, it is evident that a locally higher concentration of amorphous carbon plays an important role. For all three regions examined under electron beam irradiation, no apparent change of the DND particle size was observed during the carbon transition. The changes in the FFTs from the images are good indicators of the diminishing diamond crystallinity for these DND samples in TEM. The phenomenon of the structural transition of diamond to graphitic carbons was similar to that observed in DND-3 reported in our previous work.⁹ In that work, two possible models, “consuming diamond” and “stacking on diamond”, were proposed to illustrate the disappearance of diamond crystallinity in the core and the increase of graphitic onion shells. For this specific DND-4 sample, it appears that both mechanisms may have occurred. The conversion of sp^3 to sp^2 -type carbon bonds in NDs has been studied previously, mostly by annealing at high temperatures.^{27,33,34} These studies reported that the phase transformation of diamond to graphitic carbons proceeded inward from the outer shells to the core, reflecting our “consuming diamond” model. Our results also demonstrated that the diamond stability is surprisingly local and presumably related to the local variations in impurity concentrations. This aspect of the discussion is described in the next section.

EELS is the method to measure the conversion of sp^3 to sp^2 -type bonding that occurs for diamond upon electron beam exposure in the microscope. The C-K edge for diamond does not have the characteristic π^* -peak of graphitic and amorphous carbon that would otherwise indicate the presence of sp^2 bonding. Since the microscope used here is not aberration corrected in STEM mode, it is not capable of high-resolution imaging, although EELS data can still be collected. The beam exposure is different between the TEM and STEM modes of operation. It is relatively easy to determine in the TEM mode as discussed previously, but not so

for the STEM mode. In STEM mode, the exposure is dependent upon the size of the probe, the current in the probe, the dwell time, the number of pixels in the frame of image acquired, as well as the total time in which the area is scanned. The beam exposure is also dependent on the magnification because the probe can be smaller than the pixel size (at a low magnification), comparable to the pixel size (at an intermediate magnification), or larger than the pixel size (at a high magnification). In addition, the current density of a STEM probe is extremely high compared to the TEM mode, so stopping the focused probe can quickly cause damage and transform the sample. In practice, the sample is first imaged at a relatively low magnification to find the area of interest and then the image is zoomed in at a higher magnification to acquire the EELS data within a short time (on the order of a few seconds). Although this further complicates the issue of beam exposure in the STEM mode, it can minimize the carbon phase change in the DND sample.

Therefore, we can still estimate the approximate exposure in the scanned and acquisition area using the previously mentioned principles. First, the probe current density is estimated by dividing the probe current by the area of the probe. For our microscope, a 0.2-nm probe has a current of approximately 85 pA. This probe size is our smallest available probe and is suitable for imaging and is adequate for EELS acquisition of the C-K edge of a DND sample. However, a larger probe with higher current was used for EELS because it leads to spectra with less noise due to the increased number of counts. Assuming a perfectly circular shape of electron beam, the 0.2-nm probe size gives a current density of approximately 2.7×10^{17} pA/cm² in an area of 0.0314 nm². For a 0.7-nm probe size beam, the current density would be approximately 9.8×10^{16} pA/cm² in an area of 0.385 nm². These values are about 4 orders of magnitude higher than the current density determined in TEM mode described earlier. While collecting spectra, a preview scan area of 512 × 512 pixels with a dwell time of 4 μs is used and the total frame time is approximately 1 s. The area fraction of the probe size to the scanned area must also be considered. For example, the scan area is approximately 5.2×10^4 nm² at a 2-million (2 MX) magnification, which gives an area fraction of 5.2×10^{-6} and 6.4×10^{-4} for a 0.2- and 0.7-nm probe, respectively. Multiplying the probe current density by the area fraction, the time per frame, and the number of frames will give the exposure (pA·sec/cm²) during scanning in an area where the spectra are collected. The exposure determined at a low magnification and at a high magnification can then be estimated. Table 1 shows the probe area fractions calculated for different probe sizes at several magnifications. The current densities of the probe are similar regardless of the different sizes at about the order of 1×10^{17} pA/cm². However, their area fractions can change over 5 orders of magnitude and the probe area can become an appreciable portion of the scanned area at larger magnifications. Thus, the electron exposure becomes significantly large at high magnifications, and can

convert the DND to the graphitic phase more rapidly than at low magnifications. Table 2 shows the calculations for beam exposure using the area fractions from Table 1 for different probe sizes and magnifications at three different scanning times for comparison. The values in this table can be a good reference for understanding the stability under STEM conditions when compared to TEM imaging conditions. In TEM, the phase changes in a DND sample became readily apparent in the stable regions after about 10 min while imaging at high resolution. The typical calculated exposure after 10 min in TEM mode is approximately 9.6×10^{15} pA·s/cm². The values in Table 2 that are about the same or higher than this are indicated in red. Using this value as a guide, this exposure is not reached in STEM for the smallest probe unless an extremely high magnification is used with stationary probe. For larger probe sizes, one must be careful to stay at lower magnifications or the phase transformation can occur more rapidly. In general, the samples will remain stable when imaging in the STEM mode. However, if hydrocarbon contaminants are present, as seen in some regions in the DND sample, the high current density exposed in STEM can exacerbate the contamination, leading to even more rapid increases of the contaminant signals in the EELS data.

Table 1 STEM probe area fraction (probe area/scan area)

Probe (nm)	Current (pA)	Area (cm ²)	Current density (pA/cm ²)	800 k× Area fraction	2 M× Area fraction	15 M× Area fraction	25 M× Area fraction
0.2	85	3.1×10^{-16}	2.7×10^{17}	8.3×10^{-07}	5.2×10^{-06}	2.9×10^{-04}	8.1×10^{-04}
0.7	375	3.8×10^{-15}	9.7×10^{16}	1.0×10^{-05}	6.4×10^{-05}	3.6×10^{-03}	9.9×10^{-03}
1.0	777	7.9×10^{-15}	9.9×10^{16}	2.1×10^{-05}	1.3×10^{-04}	7.3×10^{-03}	2.0×10^{-02}

Table 2 STEM beam exposures

Probe (nm)	800 k \times exp (pA \cdot s/cm ²)	2 M \times exp (pA \cdot s/cm ²)	15 M \times exp (pA \cdot s/cm ²)	25 M \times exp (pA \cdot s/cm ²)
30 s				
0.2	7.1×10^{12}	4.4×10^{13}	2.5×10^{15}	6.9×10^{15}
0.7	3.1×10^{13}	2.0×10^{14}	1.1×10^{16}	3.1×10^{16}
1.0	6.5×10^{13}	4.0×10^{14}	2.3×10^{16}	6.3×10^{16}
2 min				
0.2	2.8×10^{13}	1.8×10^{14}	1.0×10^{16}	2.8×10^{16}
0.7	1.2×10^{14}	7.8×10^{14}	4.4×10^{16}	1.2×10^{17}
1.0	2.6×10^{14}	1.6×10^{15}	9.1×10^{16}	2.5×10^{17}
10 min				
0.2	1.4×10^{14}	8.8×10^{14}	5.0×10^{16}	1.4×10^{17}
0.7	6.2×10^{14}	3.9×10^{15}	2.2×10^{17}	6.1×10^{17}
1.0	1.3×10^{15}	8.1×10^{15}	4.5×10^{17}	1.3×10^{18}

Note: The values in red are the estimated exposures higher than the typical value of $\sim 9.6 \times 10^{15}$ pA \cdot s/cm² after a 10-min exposure in TEM mode.

Using the STEM imaging considerations discussed previously, EELS data were acquired to demonstrate the initial diamond structure with little sign of graphitic carbon present as shown in Fig. 4. Figure 4a shows a STEM bright field (BF) image acquired at 2 M \times with an indicated area corresponding to a magnification of 15 M \times , typical of an EELS spectrum acquisition that would sample a single particle. As noted previously, EELS spectra were acquired in STEM HAADF mode. Figure 4b shows an EELS spectrum of the C-K edge at 284 eV from a freshly viewed area that shows a very small π^* peak at 285 eV indicating that the phase is nearly pure diamond composed of sp³-C bonds. The nearly pure diamond structure also underscores that the trace graphitic carbons in this sample come from the outermost shell of the diamond particles due to surface reconstruction. Figure 4c shows a sequence of overlaid EELS spectra showing the change in the C-K edge structure with increasing electron beam exposure. The data in Fig. 4c were acquired with a 1-nm probe at a magnification of 15 M \times with the exposure times given in the legend. The growing π^* peak, indicating the increase in the sp²-C bonding characteristic of graphitic and amorphous carbons, can be seen increasing while the σ peak at 292 eV decreases.

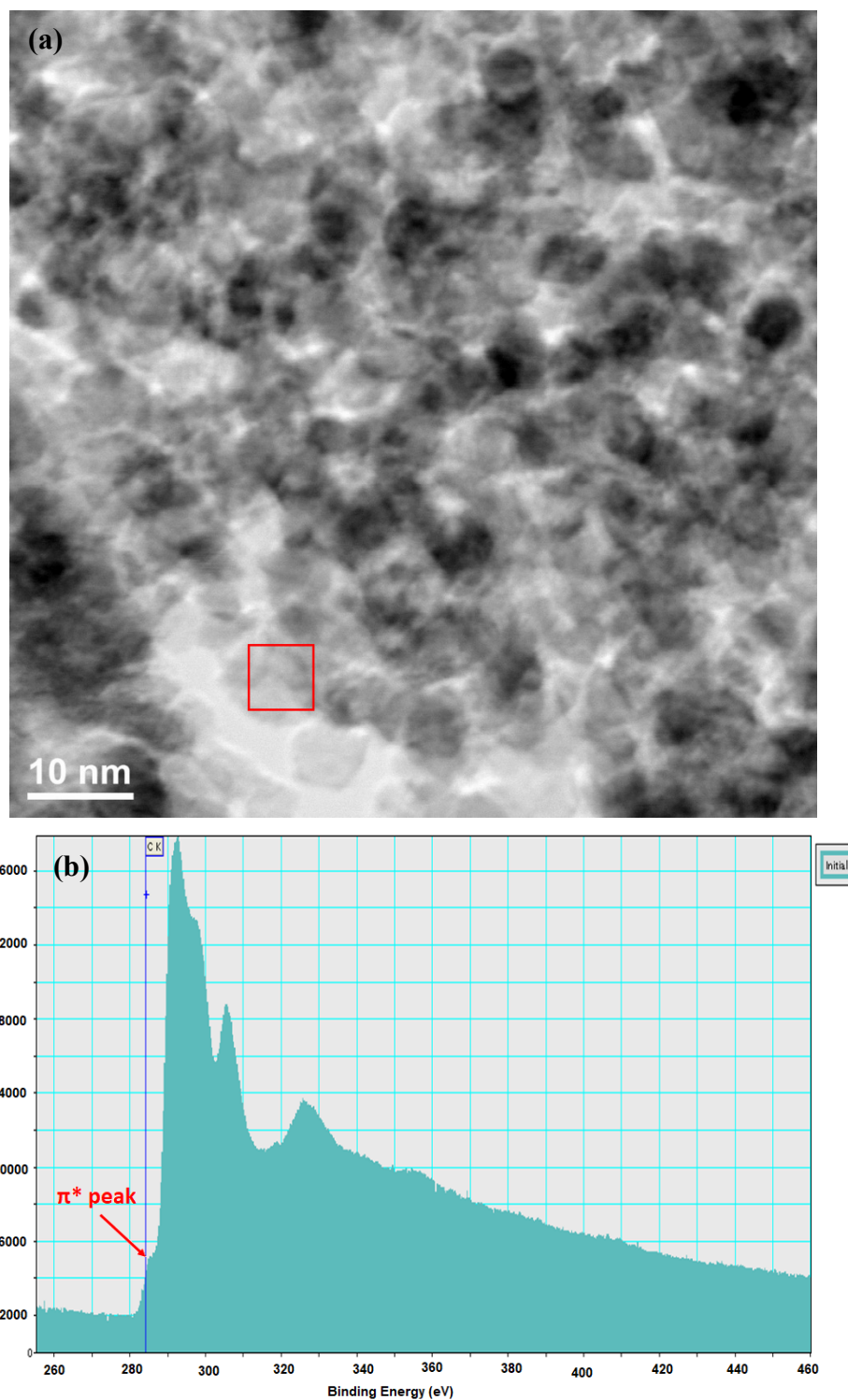


Fig. 4 STEM EELS of DND-4. a) BF STEM image of DND-4, acquired at a magnification of 2 M \times . The red box indicates an area that would be scanned at the 15 M \times magnification and suitable for acquiring EELS spectra. b) EELS C-K edge spectrum acquired from a freshly exposed area using a 1-nm beam at 15 M \times . c) A sequence of spectra acquired during scanning using a 1-nm probe at 15 M \times that shows the increasing π^* peak with a decreasing σ peak.

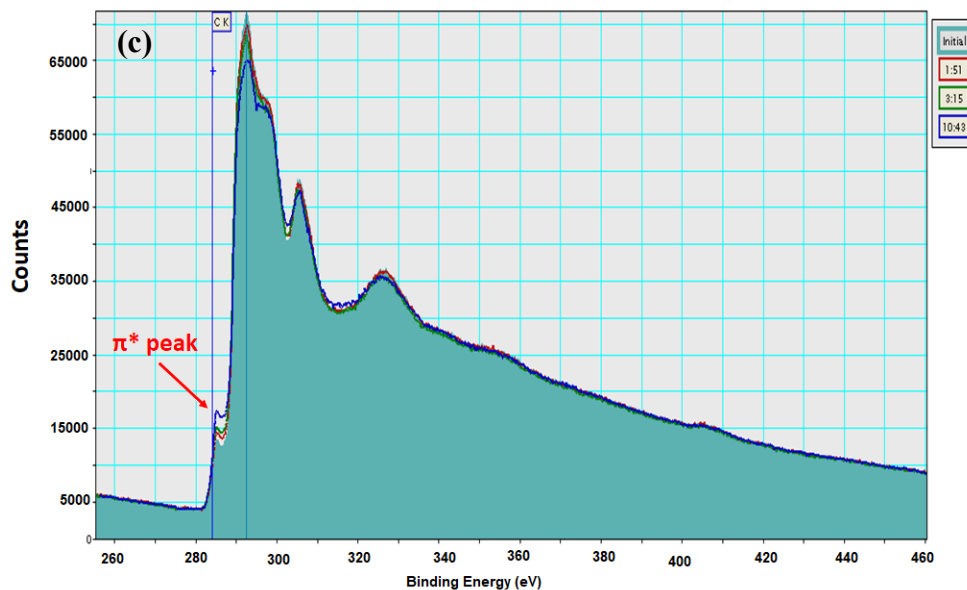


Fig. 4 STEM EELS of DND-4. a) BF STEM image of DND-4, acquired at a magnification of 2 M \times . The red box indicates an area that would be scanned at the 15 M \times magnification and suitable for acquiring EELS spectra. b) EELS C-K edge spectrum acquired from a freshly exposed area using a 1-nm beam at 15 M \times . c) A sequence of spectra acquired during scanning using a 1-nm probe at 15 M \times that shows the increasing π^* peak with a decreasing σ peak. (continued)

In all DND samples, we occasionally identified particles that were several times to even 10 times larger than the average size (~ 5 nm) and found that they still appeared to be single crystals. The existence and source of such large DND particles were discussed in our previous work (Section 3.3 and Fig. 8 in Wu et al.⁹). It is known that the final grain size of DND can vary from the experimental conditions in any step during the detonation synthesis, purification, and handling processes.¹⁴ Although commercial DNDs are assumed to contain only primary particles having average sizes of only several nanometers after grinding and sonication, the van der Waals and electrostatic forces holding the primary aggregates (in the range of several hundred nanometers) can be hard to overcome with insufficient sonication. Furthermore, experiments and models have also been conducted to demonstrate that the smaller the particle size of the explosives employed during detonation, the smaller the size of the resulting DND final products.^{17,35}

3.2 New Information on Elemental and Hydrocarbon Impurities

The broadband LIBS spectra displayed in Fig. 5 contain major emission features associated with the carbon-related elements and organic impurities in the DND samples (e.g., carbon [C], the cyano radical [CN], diatomic carbon [C₂], and hydrogen [H]). The oxygen (O) and nitrogen (N) signals contain contributions from

the air entrained in the laser-induced plasma. As seen in the figure, lithium (Li), Ca, Na, and K were observed in all DND samples. Multiple Cu emission lines were only observed in the DND-3 sample and the signal was reasonably strong for an impurity. The broadband emission around 500–700 nm is due to photoluminescence from the excited DND.³³ Similar to what we had observed before,⁹ Si, magnesium (Mg), Fe, Al and Ti were also identified in the LIBS spectra for all DND samples, as shown in Fig. 6 for these selected regions. As stated in the previous work,⁹ Si is common in DNDs even in small quantities. The DND-3 sample apparently contained the most metal impurities among all samples examined while the DND-1 sample possessed the least. All the identified metallic impurities were estimated to be less than 100 ppm in the bulk samples (tens to hundreds of micrograms sampled per laser shot).

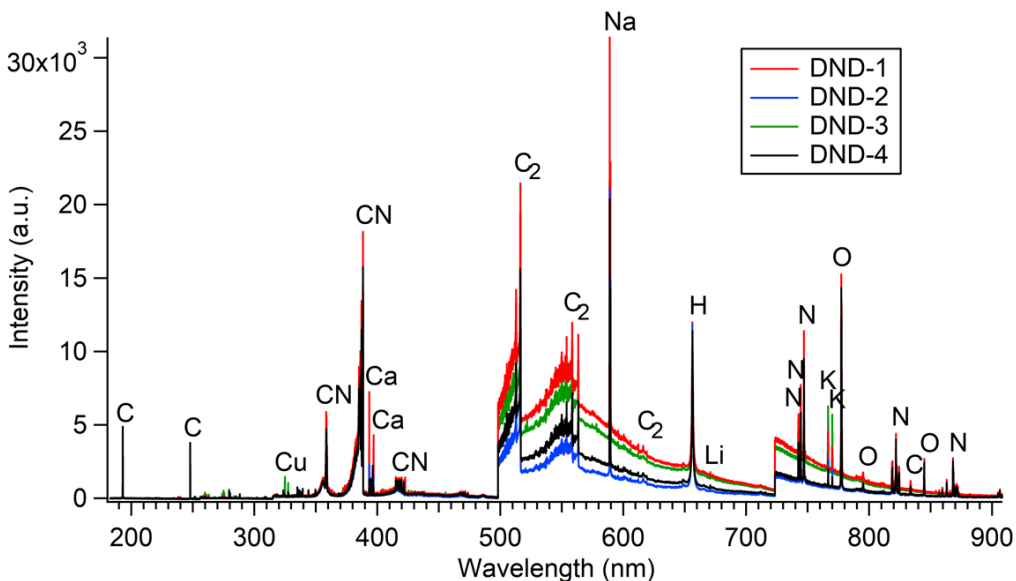


Fig. 5 LIBS spectra of all DND samples with major emission features labeled

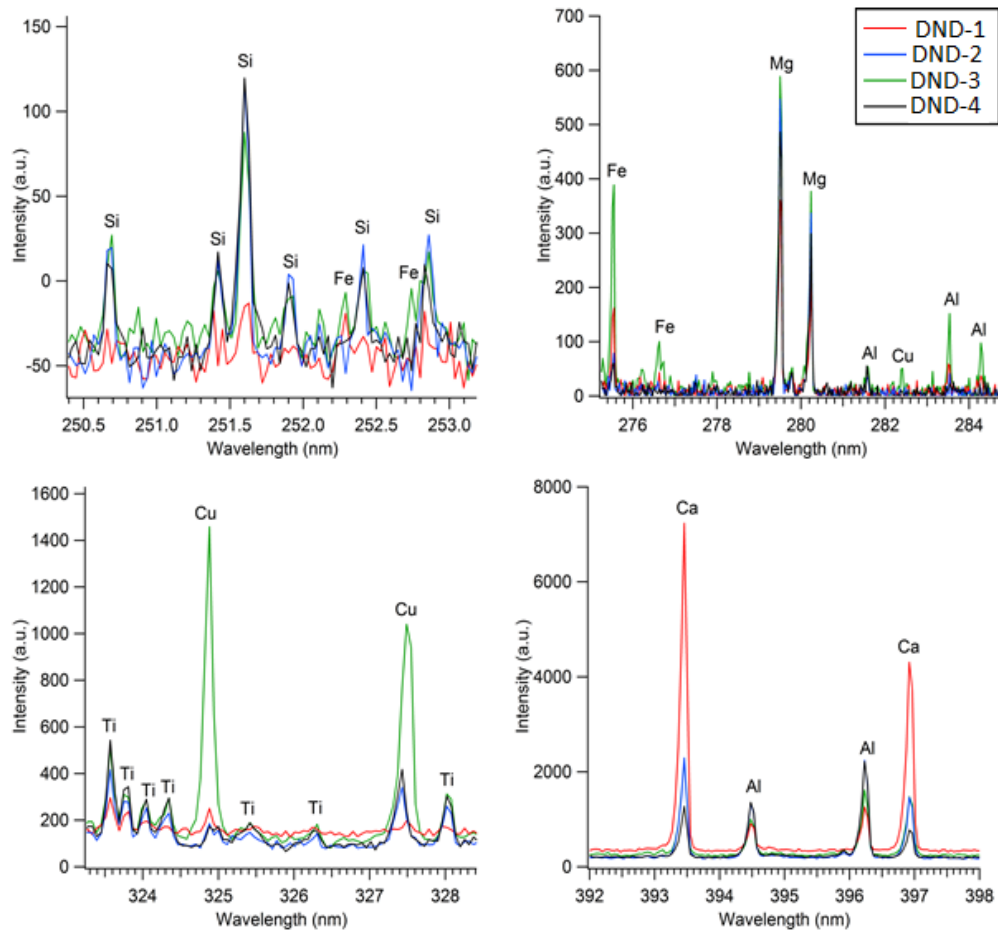


Fig. 6 Selected regions of the LIBS spectra among the four DND samples showing trace impurities such as Si, Mg, Fe, Ti, Cu, and Al

The elemental impurities were also examined via TEM-XEDS for comparison. In general, the Cu impurity cannot be determined due to the presence of the Cu peak originating from the TEM specimen grid. Small sulfur (S) peaks were identified in some of the samples (DND-1 and DND-3) but were not observed by LIBS since S is challenging to detect in trace quantities via LIBS in air. By comparing the results to the background, Co was tentatively identified in the DND-3 sample, which was not observed in any of the LIBS spectra despite a limit of detection less than 0.1 ppm.³⁶ The elements Al, Si, Ti, and Fe were identified by TEM-XEDS, which was consistent with the LIBS results. The results of the comparison of the elements found between the LIBS and TEM-XEDS techniques agreed with those found in the previous work.⁹

Although the volume of the sample measured by XEDS is limited in scale in this case, a wide range of sample volume can technically be examined depending on the area scanned by the probe, which can vary from 10s of microns along a square

image width to the nanometer scale of the static probe. To demonstrate, Fig. 7 shows several TEM-XEDS spectra that were acquired at different regions along with their corresponding TEM images. Fig. 7a is a spectrum acquired from the support film without the DND sample to account for the peaks originated from the background and their relative intensities. It is difficult to determine possible trace elements in the carbon support film on the TEM Cu grid in addition to those shown in Fig. 7a. If any trace element were originated from the support film or the TEM specimen holder, they would have either appeared or contributed equivalently in Fig. 7b–d. These spectra correspond to areas at different magnifications to represent the various sizes of the sampling areas using the DND-4 sample as an example. As anticipated, the image in Fig. 7d exhibits distinct faceted DND grains, which is a common morphology for most DND samples at a high magnifications. By comparing these background peaks to those in the sample, Fe and phosphorous (P) peaks appeared in all spectra but Ti and S only appeared in spectra acquired from relatively larger regions at a relatively low magnification—thus they are likely present at only trace levels (Fig. 7b and 7c), consistent with LIBS results (Fig. 6). Although LIBS is able to detect all elements and the only limitations are the laser power, wavelength range, and sensitivity of the detector,³⁷ like S, P is difficult to detect if the concentration is very low (as indicated by the TEM-XEDS spectra). A trace Ca signal was observed in Fig. 7b but not Fig. 7c and 7d. However, the spectra in Fig. 7 confirmed the existence of local variations of impurities, including the types and concentrations among different regions of the same sample. As a result, several elemental impurities, such as Ti, Ca, P, and S, were only detectable when spectra of relative large areas were acquired at low magnification (Fig. 7b and 7c). As discussed previously, these impurities can be introduced during purification.

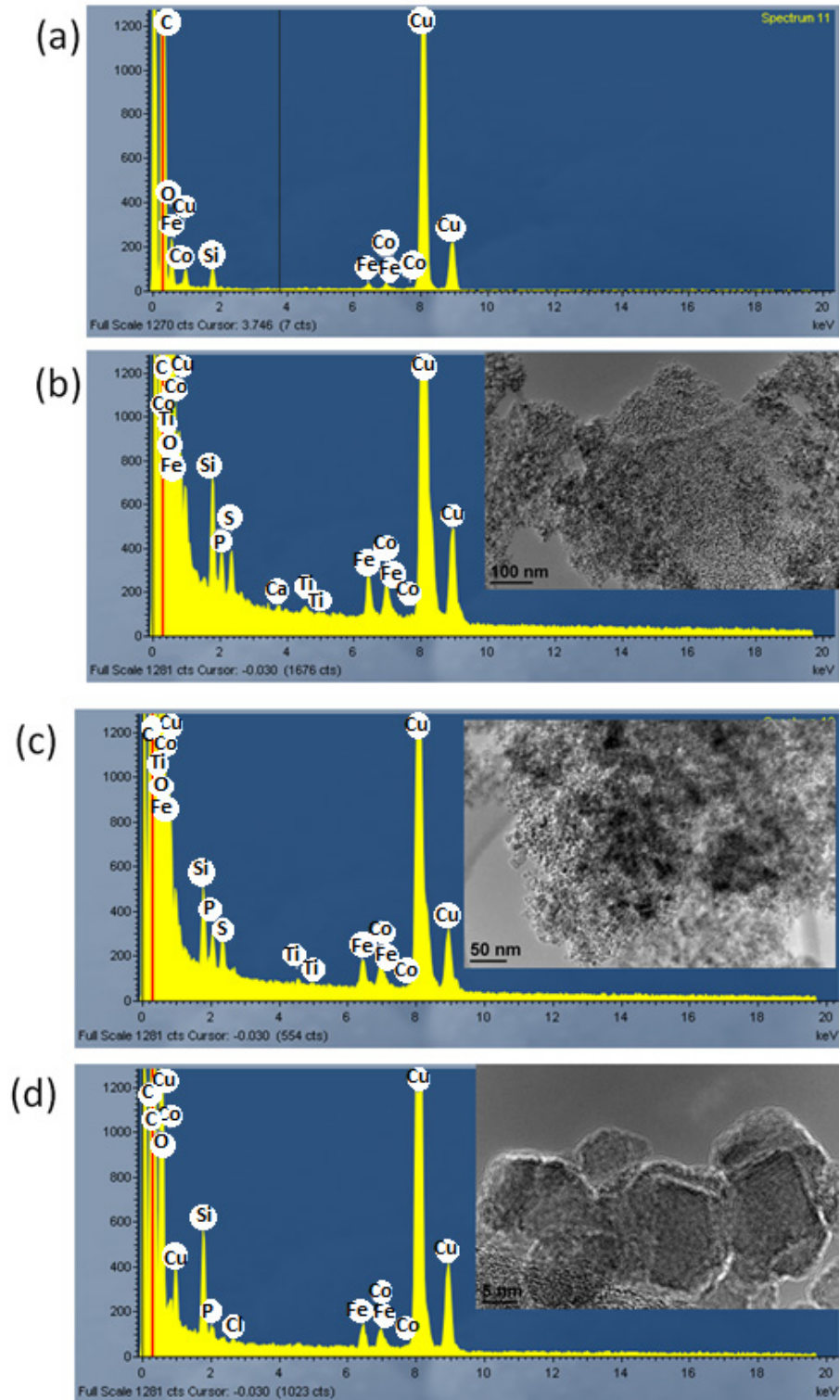


Fig. 7 The TEM-XEDS spectra acquired from different regions in the DND-4 sample along with their corresponding TEM images: a) the background, b) and c) at relatively lower magnifications, and d) at a high magnification

Given the macroscopic nature of LIBS analysis, the resultant elemental emission features are more representative of bulk composition than those from TEM analysis. Multiple elemental impurities in commercial DND samples have been demonstrated by previous studies.¹⁴⁻¹⁷ We have shown that various types and concentration levels of these impurities exist not only among different DND samples from the same source and product number but also within a single sample. The Fe impurity of our samples most likely came from detonation synthesis^{16,17} and the Na might have been introduced from sodium hydroxide (NaOH) added to neutralize the sample after the strong acid oxidation and/or from sodium salt added to improve colloidal stability.³⁸

Our previous studies on samples DND-1, DND-2 and DND-3 suggested a strong correlation between the diamond crystalline core and structural instability and the surface functional groups.⁹ In that study, we found that low contamination was correlated with stable diamond cores (i.e., DND-1 was both relatively pure and stable, while DND-3 was relatively impure and unstable). Figure 8 displays FTIR reflectance spectra for all four samples. All samples contained some level of amorphous carbon, while DND-4 had the least, as evident from the broad peak between 1500 and 1000 cm^{-1} . However, the more prominent peaks appearing for DND-2 and DND-3 indicated higher concentrations of functional groups in these samples, especially the aliphatic hydrogens (C-H near 2800 cm^{-1}) and oxygen-containing bonds near 1050 cm^{-1} . The aliphatic C-H stretching around 3000 cm^{-1} is most likely wax. The alcohol (C-OH) peak near 1400 cm^{-1} may have been introduced during the detonation synthesis and purification process.³⁹ It is also possible that it resulted from exposure of samples to air, leading to surface-absorbed water molecules and hydroxyls. As indicated in Fig. 8, the concentration of organic contaminants for DND-1 and DND-4 was much lower than DND-2 and DND-3. As previously discussed,⁹ spectra of these “dirty” DND samples suggested contamination by wax and surfactant surfactants in the solution.^{40,41} The higher organic contaminant content in DND-2 and DND-3 also led to comparatively lower “quality” for these samples with respect to the ratio of diamond carbons to non-diamond carbons (graphitic and amorphous) and the overall relatively unstable diamond cores.⁹ The relationship between the stability of diamond crystallinity, as described in Section 3.1, and the organic contaminants in the relatively “good”-quality DND samples, such as DND-1 and DND-4, were also reconfirmed by the XRD results, which is discussed in Section 3.3. Overall, the FTIR spectra shown in Fig. 8 and their implications for the chemical compositions and functional groups were consistent with previous reports for different types of NDs (e.g., Motahari and Malekfar⁴²).

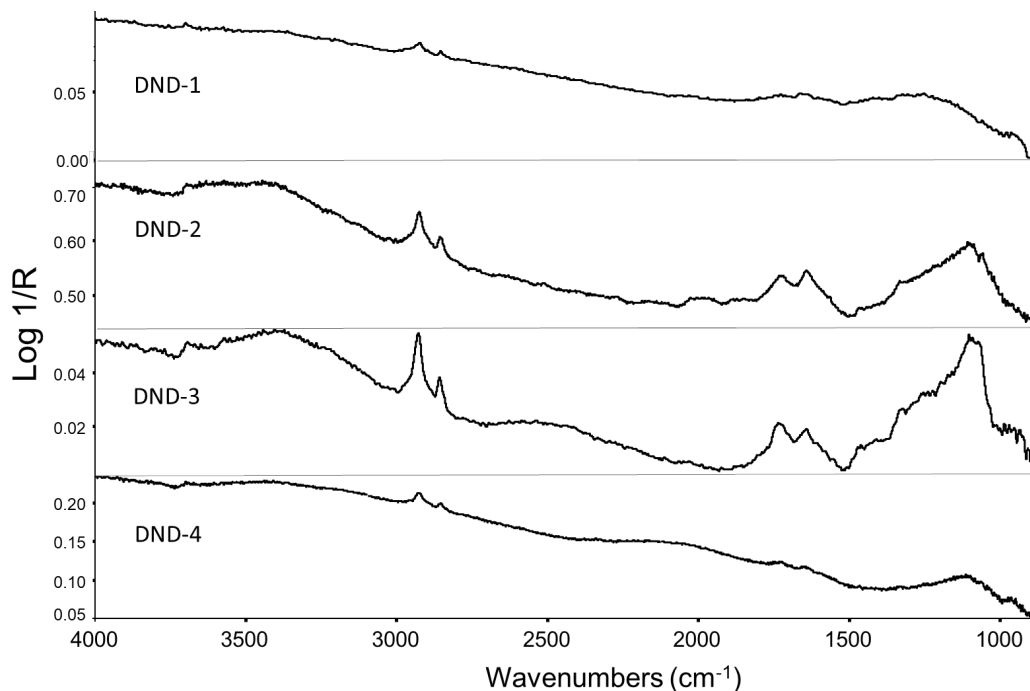


Fig. 8 FTIR-microscope spectra of all DND samples

3.3 Powder X-ray Diffraction (XRD) Studies

The XRD spectra for all DND samples examined in this work are shown in Fig. 9. As anticipated, the diamond crystalline structure was illustrated by the major peak at $2\theta \sim 44^\circ$ corresponding to the $\{111\}$ diffraction plane along with two relatively low-intensity peaks at $2\theta \sim 75^\circ$ and 91° , corresponding to the $\{220\}$ and $\{311\}$ diffraction planes, respectively (Powder Diffraction File [PDF] card file number 01-071-3649).^{43,44} The XRD spectra for diamond-related material have been reported in the past and shifts in the peak position were found to be closely related to the microstructure when the same X-ray source is used. The peak positions are also related to the particle size for NDs and thickness for diamond film,⁴³ which seemed to be the case when our XRD data were compared with previous reported work. The shift of our XRD peaks were found to be insignificant when compared with those reported by Roy and coworkers⁴³ and Pang and his colleagues⁴⁴ but significant when compared to those using a Co X-ray source, as reported by Motahari and Malekfar.⁴² In general, our spectra matched well with the diamond carbon structure in the database but with a broadening effect on the $\{111\}$ diamond major peak due to the presence of polymeric alkene contaminants, as shown in the zoomed XRD spectrum (Fig. 9b). This also reaffirmed our FTIR findings for the presence of aliphatic hydrogens and oxygen-containing functional groups in our previous work.⁹ The DND-3 sample exhibited a more pronounced broad peak at approximately 20° – 30° suggesting the higher content of amorphous carbon in this

sample compared to the others. Further deconvolution of all peaks suggested the elemental impurities of Fe, Ti, and manganese (Mn). The small peak at approximately 26° corresponding to the (002) graphite plane (as denoted by the red triangle) only showed up for DND-1 and DND-4 samples, which possess the most distinct diamond core structures surrounded by the onion-like graphitic shells. These finds are consistent to what reported by Pang et al.⁴⁴ in their XRD spectra acquired from diamond-like carbon films. Also consistent to Pang et al.'s report, the small peak representing carbon near approximately 36° only appeared for DND-3, which we identified as the DND sample possessing the least crystallinity and most organic contaminants in our previous work.⁹ TEM images have illustrated the distinct diamond crystalline cores surrounded by minimum onion-like graphitic carbon shells for these two samples. The small (002) graphite major peak in the XRD spectra reaffirmed the relatively minor content of graphite compared to the diamond.⁴²

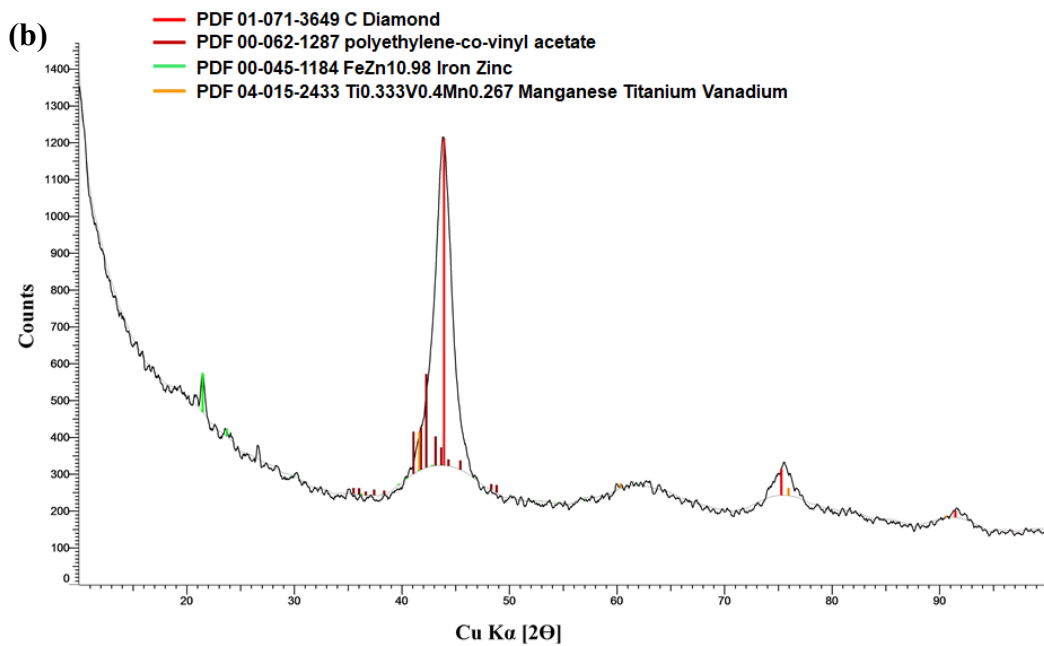
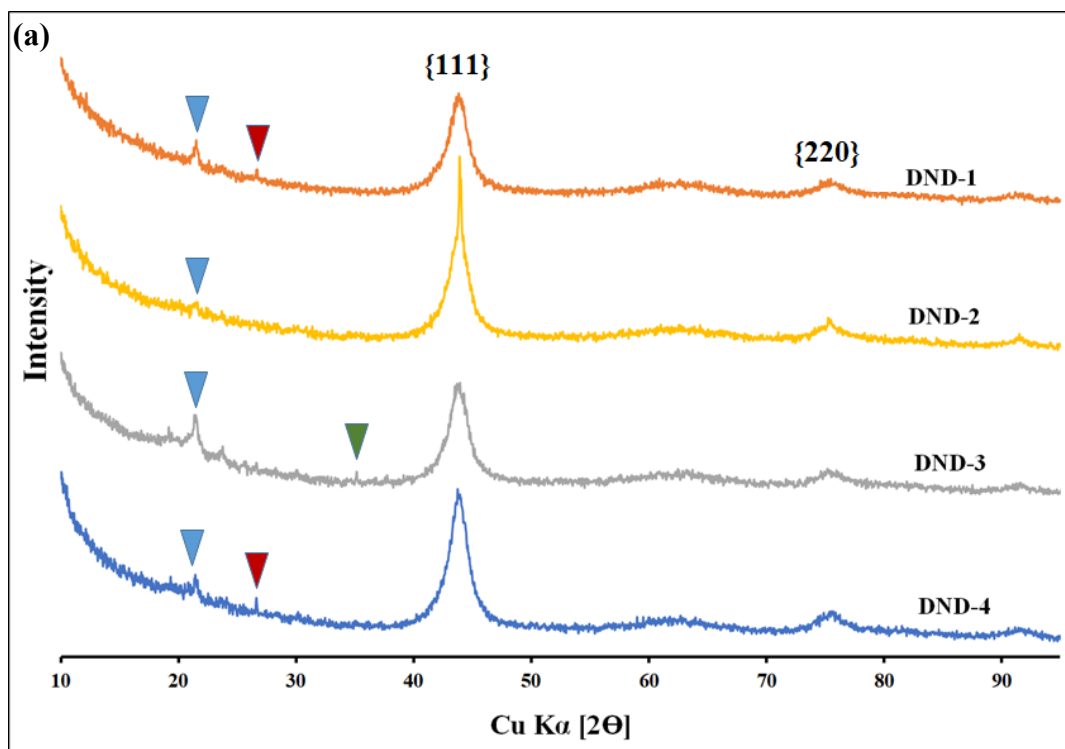


Fig. 9 XRD for all the DND samples: a) overall scan from 10° to 95° and b) a zoomed spectrum to show the deconvoluted peaks for a diamond XRD spectrum

3.4 Small-Angle X-ray Scattering (SAXS)

The corrected SAXS data for all four DND samples are given in Fig. 10, shifted vertically for clarity. All samples exhibit a Guinier “knee” centered around 0.07 \AA^{-1} , no form factor fringes, and a significant low-angle upturn typical of materials containing NPs and aggregates thereof.⁴⁵ The unified model developed by Beaucage, which combines the Guinier approximation with the Porod’s law as given in Eq. 1, has been widely and effectively used to fit data of these kind.^{20,45} In Eq. 1, the first term is the Guinier component, scaled by a prefactor G . The second term is a modification of the Porod’s law, where B is a scaling factor, P is the Porod’s law exponent, q^* is defined as $q^* = q/[\text{erf}(kqR_g/6^{1/2})]^3$, and in which k is a constant involved in the low- q power law limit.²⁰ Fitting the data for a smooth NP surface would yield value of 4 for P .

$$I(q) = G \cdot \exp\left(\frac{-q^2 R_g^2}{3}\right) + B \cdot (q^*)^{-P} \quad (1)$$

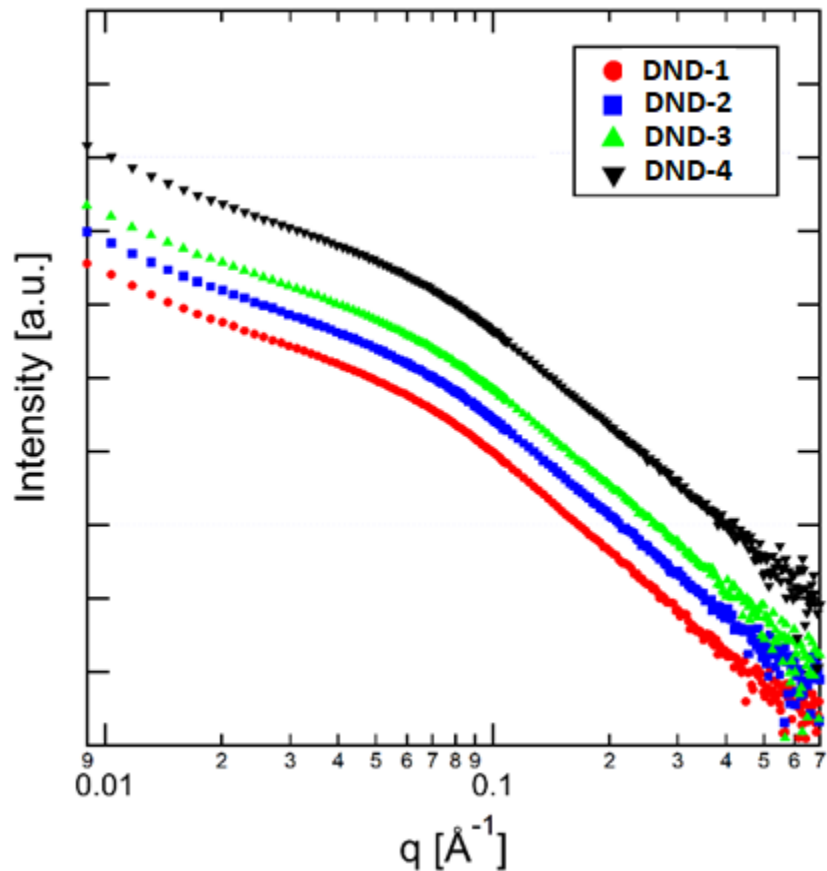


Fig. 10 SAXS data for each of the four DND samples in this study. Data are shifted vertically for clarity.

Figure 11 illustrates the use of the unified approach to fit the data from DND-1. The results of the unified model fitting for all samples are listed in Table 1. These values are somewhat larger than those determined from the TEM data and previous literature, with an R_g of approximately 40 Å, corresponding to an NP diameter of approximately 8 nm. The values of the Porod's exponent given in Table 3 all exceed 4, indicating diffuse interfaces between the DND NPs and matrix. Notably, the typical value of approximately 4.6 observed here is greater than that reported in the literature,²⁶ where 4.2 was more common. This additional negative deviation from Porod's law behavior may be attributed to the presence of low-molecular-weight “wax” or dispersing agent residue,⁹ providing additional texture on the DND surface. A trace S peak identified in the TEM-XEDS data, the presence of sodium dodecyl sulfate indicated via gas chromatography-mass spectrometry in our previous work,⁹ and the presence of surface functional groups as identified via FTIR in that work are evidence that a S-containing surfactant may have been used in the manufacturing process and may be present in these four samples.

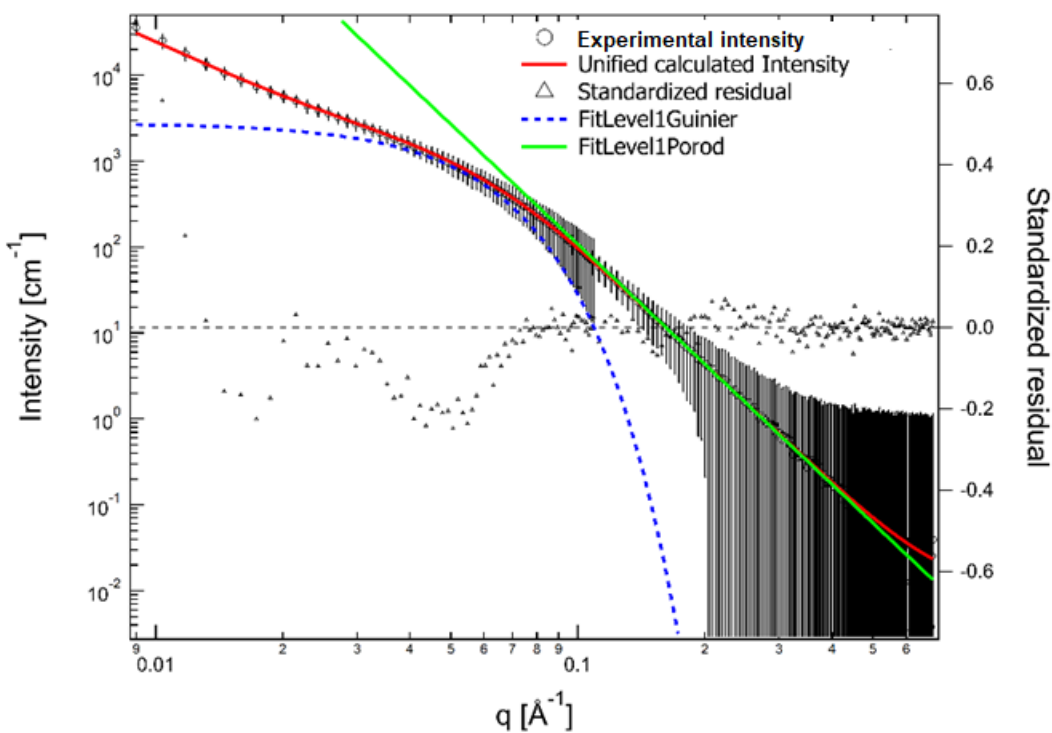


Fig. 11 Results from fitting the SAXS data for DND-1 using the unified model, comprising a Guinier approximation and a Porod's law term

Table 3 Results from fitting the SAXS data with the unified model and a core-shell form factor. Here P corresponds to the Porod's exponent in Eq. 1.

Sample	Unified R_g (Å)	Unified P	Core-shell core radius (Å)	Core-shell core radius std dev (Å)	Core-shell thickness (Å)	Core-shell total particle R_g (Å)
1	37.1	4.64	25.8	16.2	7.16	29.0
2	39.7	4.60	25.4	16.5	6.55	28.7
3	40.3	4.60	24.9	16.1	6.46	28.1
4	39.6	4.52	25.5	16.6	6.05	28.8

To facilitate modeling the scattering data from the primary NP due to agglomerations and the diamond/graphite core/shell structure, the low-angle upturn was fit using a power-law function where $I(q) \sim q^{-2.4}$; the exponent was determined empirically. Although the unified model fits the data well, the use of the Guinier approximation limits the information on the NP that can be derived to an average radius of gyration value and overestimates the DND size. Here, because DNDs are well-known to have a core-shell structure, additional information may be obtained through the use of a form factor for a sphere having a core-shell electron density function.⁴⁶ Using a density of 3.515 g/cm³ for the diamond core, and 2.230 g/cm³ for the graphite shell layer, X-ray scattering length density (SLD) values of $29.8 \times 10^{10} \text{ cm}^{-2}$ and $18.9 \times 10^{10} \text{ cm}^{-2}$ were calculated for diamond and graphite, respectively, which is close to those used by Moore¹⁹ and Mykhaylyk et al.²⁷ The SLD of the matrix or solvent phase, required for the form factor calculation, was set to zero. A Gaussian distribution of DND NP core radius was assumed. As with the unified model fitting, the low-angle upturn was modeled with a power-law function determined empirically, with intensity scaling as $q^{-2.4}$.

Figure 12 shows the results of fitting a core-shell form factor to the SAXS data for DND-4. The core radius, shell thickness, and standard deviation of the core radius are reported in Table 3. All four samples had approximately the same average particle radius, approximately 31.5 Å, and radii of gyration values of approximately 28 Å. These data are in excellent agreement with the measurements from TEM micrographs.

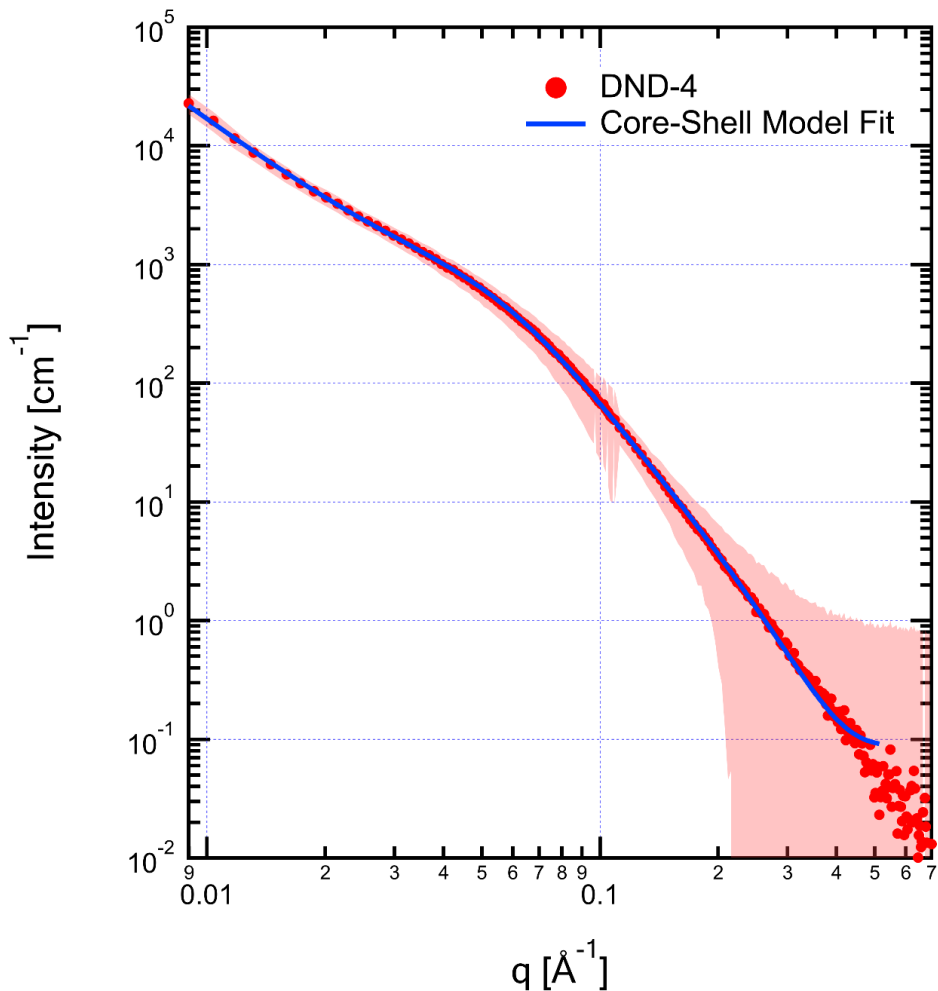


Fig. 12 SAXS data for DND-4 and the results of modeling the scattering data using a core-shell form factor. Error bars are shadowed for clarity.

3.5 Zeta Potential Measurement and Particle Size Distributions

Table 4 exhibits an overall summary of the data obtained from the zeta potential measurements and particle size distributions for all samples. Zeta potential is a characteristic for evaluating the colloidal stability of NPs in solution. The zeta potentials of all our DND samples were measured between +10 and +20 mV, comparable to the +11.2 mV reported by Motahari and Malekfar for NDs⁴²; the value for DND-4 in water suspension is comparable to the three previous samples.⁹ This finding also confirms that the particle instability in dispersions of all our DND samples is independent of the level of amorphous carbon and impurity content. The standard deviations for the measured zeta potentials for all samples were around 20%–30% from the mean value. Overall, the measurement was of good quality, with the individual measurements for each sample overlapping with each other. It is known that the magnitude of the zeta potential can indicate the degree of

electrostatic repulsion between charged particles in a dispersion and these results support our previous conclusion of tightly agglomerated particles as evident from the TEM images.⁹

Table 4 Zeta potential measurement data for all DND samples

Sample	Zeta potential (mV)	Z-average (nm)	Size (nm)	Percentage (%)
DND-1	16.6 ± 4.56	286.8	272.7	76.5
			1728.0	20.9
			4870.0	2.6
DND-2	9.29 ± 4.36	724.6	729.9	80.4
			4616.0	19.6
			0.0	0.0
DND-3	15.2 ± 3.80	803.0	1877.0	76.0
			300.3	24.0
			0.0	0.0
DND-4	12.3 ± 3.70	490.2	496.0	73.3
			2640.0	26.7
			0.0	0.0

Other previous studies^{47,48} have also measured positive zeta potentials for commercial DND in water solution similar to ours. Several approaches during purification and sonication fractioning have also been attempted to increase the zeta potential of DND particles reaching absolute values in the range of 50–100. For example, Osawald⁴⁹ used oxygen annealing to remove the carbon contaminants, Gibson et al.³⁸ added sodium salt, and Shenderova et al.⁵⁰ used ozone purification to facilitate the decomposition of carboxylic anhydride surface functional groups. In particular, the work conducted by Shenderova et al. led to particles not only stable over a broad range of pH values (2–12) but also with a smaller Z-average particle size of 160–180 nm in water suspension, which is two to three times smaller than our DND samples and near the reported diameter of DND core aggregates.⁵⁰ Moreover, metallic and non-metallic contaminants have the tendency to facilitate DND particle aggregations.¹⁵ Turner et al.¹⁰ suggested that DNDs having larger agglomerations show comparatively higher content of non-carbon elements such as H, N, O, ashes, and amorphous carbon. Ozawa et al.³⁴ suggested that considerable surface forces and chemical bonding due to organic surface functional groups would facilitate the agglutination and oxidation effects. Motahari and Malekfar suggested that a positive zeta potential can be attributed to more hydrogen presence on the surface relative to oxygen.⁴² Although the agglomeration of DND in air is mainly dependent on the van der Waals molecular force, which is different from the electrostatic forces in solution such as water, our relatively low zeta potentials still indicate the agglomerated nature of our DND samples. Moreover, the zeta potential measurements were also consistent with the results found by the other techniques used in this work.

The agglomeration nature of all DND samples was confirmed by the measured particle sizes via dynamic light scattering (DLS). The decay for the varying fluctuation rate of a dynamically scattered light source due to the presence of particles in the solution is related to the particle size and resultant Brownian motion and defined as the correlation function to be used to calculate the particle size distribution. In general, the intensity of scattering of a particle is proportional to the sixth power of its diameter based on the Rayleigh's approximation, hence the scattering of light is more pronounced for large particles than small particles.⁴⁷ Figure 13 shows the size distributions by intensity of all DND water suspensions along with the data from graphite nanoparticles (GNPs) that are known to have a similar particle size distribution as our DND samples. Our particle size data were results over three repeat measurements for each sample. As clearly shown in the figure, the measured distributions indicated the bimodal nature of all DND samples and GNPs with each sample generally exhibiting two to three broad peaks with zeta potential-derived size distributions; the range is 2–3 orders higher than those observed by TEM. The results also support the anticipated tightly agglomerated nature of the DND samples and GNPs in water suspensions. Notice that the GNP suspension had a comparatively narrow monomodal distribution in one experiment. The finding of multiple peak distributions for NDs had also been reported by Motahari and Malekfar.⁴² They measured a peak between several tens to hundreds of nanometer in the first distribution and a smaller second peak reflecting a size distribution in the micrometer range for two different samples. These two distributions resulted in average particle sizes reflecting agglomerations.

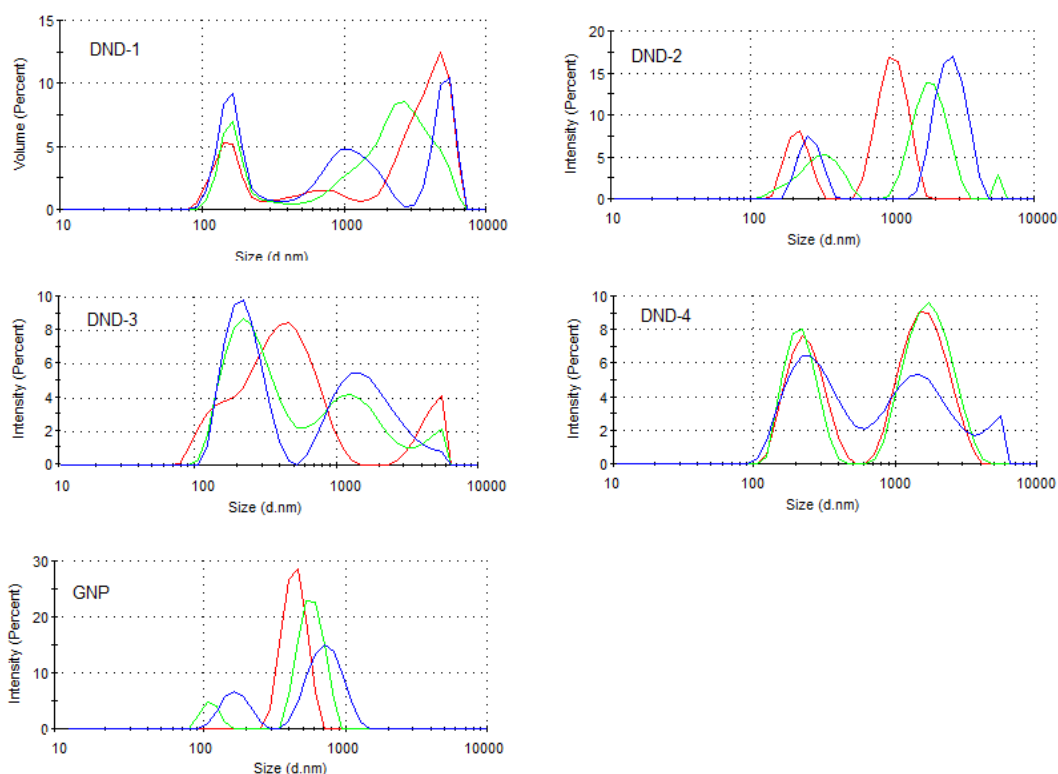


Fig. 13 Size distributions by scattered light intensity of DND suspensions (0.05–0.1 wt% in deionized water); each color represents the results obtained from one repeat experiment for each sample.

As shown in Table 4, except DND-3, all other samples exhibited submicron-sized aggregates that accounted for more than 70% of the sample while the remaining 20–30% of the sample consisted of even larger aggregates in micron sizes. For DND-1, a third small peak appeared at nearly 5 microns, accounting for only 3% of the sample, which may indicate the presence of super large aggregates or particulates in the sample or possible dust presence in the sample. Nevertheless, DND-1 still possessed the smallest Z-average diameter among all samples. In contrast, DND-3 showed an 1877-nm Z-average diameter accounting for 76% of the sample, while only 24% of the sample could be attributed to the smaller aggregates of a 300-nm Z-average diameter. Such peak distributions led to a relatively large Z-average diameter in comparison to other samples. The DND-3 sample also seemed to have the largest discrepancy in the starting correlation among all measurements, which can be attributed to its higher content of organic surface functional groups that were determined via FTIR in our previous work.

In our previous work,⁹ we had discussed the Z-average diameters for DND-1, DND-2, and DND-3, which all exhibited in the range of several hundred nanometers. The Z-average diameter of DND-4 was measured as 490 nm, which was comparable to other DND samples previously described. (The Z-average

diameters for DND-1, DND-2, and DND-3 are in the range from ~ 300 to 800 nm.) The core agglutinates in the range of several hundred nanometers in size have been widely recognized and known to be difficult to break up due to the unusually tight binding within the agglutinates for commercial DND (Osawa¹⁴). The derived diameters of the powders, in the decreasing order of DND-3 > DND-2 > DND-4 > DND-1, correlated well with the concentration of metallic and organic impurities that we previously found⁹ and further investigated in this work (Figs. 5, 6, and 8). This correlation may be attributable to the weaker binding forces among primary particles due to the presence of impurities, which facilitate particle agglomerations. The relative colloidal stabilities among these DNDs did not appear to change over a span of 4 days, as evidenced by nearly identical zeta potentials obtained. In comparison to the approximate primary particle sizes of 3–6 nm that were specified by the vendor, our measured particle sizes in water suspension were ~ almost 2 orders of magnitude larger. This finding further confirmed that tight aggregates of primary DND particles cannot be separated by sonication¹⁷ and suggests that the strong interactions between DND particles and water are due to the existence of contaminants.

4. Conclusion

Four commercial DND samples from different lots provided by the same vendor with identical product numbers were characterized by using different techniques including TEM, LIBS, FTIR, XRD, and zeta potential and particle size measurements via DLS and SAXS techniques. In contrast to our previous work identifying the bulk differences in diamond structure and instability, metallic impurities, and organic functional groups among these samples, this work put a significant emphasis on the local variations within the sample (DND-4) for which a general TEM imaging survey of different areas suggested an overall relatively high level of crystalline diamond structure similar to DND-1, a sample which was concluded as the best quality DND sample in our previous study.

FTIR spectra also revealed a relatively lower content of organic impurities and surface functional groups for the DND-4 sample, which is consistent with our previously reported correlation of high sample contamination to reduced diamond stability. Nevertheless, even for those comparatively clean samples with high concentrations of distinctly crystalline diamond cores such as DND-1 and DND-4, the local stability of the diamond structure varied significantly from one location to another within the same sample. Using DND-4 as an example, we demonstrated different deteriorations of the sp³-C in the diamond core and gradual increase of the surrounding onion-like graphitic sp²-C shell thicknesses with three randomly selected regions. In one region, the carbon conversion within a 21-min duration was

demonstrated by the changing crystallinity in TEM images, the buildup of amorphous carbons revealed in FFT, and the significantly increased [002] graphite-carbon peak in the radial average of the FFT. In another region, the faster deterioration of crystalline diamond core replaced by the increased graphitic onion-like shells within 9 min was demonstrated using approximately the same current density. In the third region, we discussed an even faster deterioration due to the increased current density. The carbon phase conversion was also measured via EELS in the STEM mode by which the spectrum clearly showed a pronounced π^* -peak of graphitic and amorphous carbons indicating the presence of sp^2 bonding after the crystalline diamond deteriorated. We also discussed the dependence of electron beam exposure on the size, current, and dwell time of the probe and the number of pixels in the frame, as well as the total time spent on the area that is scanned during STEM operation that must be considered when comparing the data with what are obtained by TEM operation.

Metal impurities such as Li, Al, Ti, and Mg were observed in all samples via LIBS; the DND-3 sample contained the most impurities, including Cu, Fe, and Si. Multiple Cu emission lines were also observed in the DND-3 sample, yet were hard to detect definitely from TEM-XEDS. No S emission features were observed in the LIBS spectra for any of the samples, despite observed features in both the DND-1 and DND-3 via XEDS; the presence of S was attributed to the S-containing surfactant in the processing. By using DND-4 as an example, the varying elemental impurities for this comparatively clean sample were locally probed and compared by changing the sampling size for XEDS acquisition. We found that several elemental impurities, such as Ti, Ca, P, and S, were only detectable when the spectra of relative large areas were acquired. Because these impurities are most likely to be introduced during the purification process in the production, their highly nonuniform distributions are consistent with the locally varying diamond stability observed by TEM.

XRD studies revealed the diamond crystalline structure with three diamond peaks corresponding to the {111}, {220}, and {311} planes for all DND samples, with a peak broadening observed on the {111} peak. Deconvolution of the major {111} peak revealed the presence of possible polymeric alkane- or alkene-group organic contaminants that were consistent with the FTIR analysis. The DND-1 and DND-4 samples also showed a small crystalline {002} graphite peak that did not appear in DND-2 and DND-3. This can be related to the distinct onion-like graphitic carbons surrounding the diamond core for these lower quality (higher impurity) samples, as revealed in TEM images. For DND-3, XRD data showed a more pronounced broad peak at approximately 20° – 30° , which was consistent with FTIR data and the XPS data suggesting a higher content of amorphous carbon.

SAXS results showed that all the samples studied had very similar primary particle sizes, as well as evidence for the formation of agglomerates of the primary NPs. The SAXS-deduced diameter of approximately 8 nm was relatively larger than the approximately 5-nm particle sizes observed by TEM. This was attributed to the greater Porod's exponent values (4.6), reflecting the diffuse interfaces between the DND particles and the matrix that might have been caused by the presence of wax or dispersing agent residue identified by FTIR. The SAXS data were further fitted by a core-shell form factor to calculate the core radius and the shell thickness, resulting in approximately the same average particle radius of 3.15 nm and radii of gyration values of approximately 2.8 nm, which are in excellent agreement with TEM observations.

The relatively low zeta potentials with all the values below 30 mV (+10 to +20 mV) for these DND samples confirmed their colloidal instabilities in water dispersions, namely, a greater electric polarization between the particle surface and the bulk medium (water). The low zeta potential values were also consistent with the sodium and organic agents that were identified by our chemical analyses via FTIR and LIBS as evidence of possible insufficient purification during processing. The particle size analysis via DLS showed bimodal distributions for all samples, showing peaks at several hundred nanometer and micrometer ranges with deduced Z-average diameters in the several hundred nanometer range that were 2 orders of magnitude larger than those of single particle grains for all samples. The results strongly indicated the tendency of interparticle agglomerations. We also found that the higher the impurity content in the sample, the larger the Z-average diameter with the order DND-3 > DND-2 > DND-4 > DND-1.

Overall, the present work successfully analyzed nanoscale variations in nominally homologous commercial DND samples using multiple independent techniques. We identified the local variations in the diamond structure and stability for the new DND sample (DND-4), which was determined to be of overall good quality with a relatively high diamond-to-graphite content ratio, similar to DND-1. Local variations in impurities were examined by comparing the XEDS data from smaller regions of the agglomerates to the overall average acquired from a larger collection view in TEM. The effort to correlate the local variations among impurity types, diamond instability, zeta potential values and bimodal particle size distributions also experimentally validated the relationship between the impurities to the resulting diamond morphology and stability. Such differences in the diamond structure, metallic and other inorganic impurities, as well as the organic contaminants identified in this work are most likely common for commercial DND products due to the difficulty in optimally controlling every step during large-scale production and purification. In conclusion, this work provided valuable insights

with experimental evidence that comprehensive characterization measures should be taken to not only verify the bulk DND sample properties but also identify the local variations in the structural and chemical properties when using commercial DND samples for potential applications.

5. References

1. Dolmatov YV. Detonation-synthesis nanodiamonds: synthesis, structure, properties and applications. *Russ Chem Rev.* 2007;76(4):339–360.
2. Schrand AM, Ciftan Hens SA, Shenderova OA. Nanodiamond particles: properties and perspectives for bioapplications. *Crit Rev Solid State Mater Sci.* 2009;34:18–74.
3. Mochalin VN, Shenderova O, Ho D, Gogotsi Y. The properties and applications of nanodiamonds. *Nat Nano.* 2012;7(1):11–23.
4. Wei AL, Liu HY, Wang FW, Li XY, Yan HY. Fabrication of nanodiamond-based composite monolithic column and its application in separation of small molecules. *J Appl Polym Sci.* 2016;133(31):43776.
5. Nunn N, Torelli M, McGuire G, Shenderova O. Nanodiamond: a high impact nanomaterial. *Current Opinion in Solid State and Materials Science.* 2017;21:1–9.
6. Zhang Y, Rhee KY, Hui D, Park S-J. A critical review of nanodiamond based nanocomposites: synthesis, properties and applications. *Composites Part B.* 2018;143:19–27.
7. Johnson DF, Mattson WD. Theoretical investigations of surface reconstruction on C nanodiamonds and cubic-BN nanoparticles. *Diam Relat Mater.* 2015;58:155–160.
8. Johnson DF, Mullin JM, Mattson WD. High-velocity collisions of nanodiamond. *J Phys Chem.* 2017;C121:1140–1145.
9. Wu C-C, Gottfried JL, Pesce-Rodriguez RA. On the structure and impurities of a nominally homologous set of detonation nanodiamonds. *Diam Relat Mater.* 2017;76:157–170.
10. Turner S, Lebedev OI, Shenderova O, Vlasov II, Verbeeck J, Van Tendeloo G. Determination of size, morphophology, and nitrogen impurity location in treated detonation nanodiamond by transmission electron microscopy. *Adv Funct Mater.* 2009;19:2116–2124.
11. Podlesak DW, Huber RC, Amato RS, Dattlebaum DM, Firestone MA, Gustavsen RL, Johnson CE, Mang JT, Ringstrand BS. Characterization of detonation soot produced during steady and overdriven conditions for three high explosive formulations. *AIP Conference Proceedings.* 2017;1793:030006.

12. Cui J-F, Fang X-W, Scjmidt-Rohr K. Quantification of C=C and C=O surface carbons in detonation nanodiamond by NMR. *J Phys Chem C*. 2014;118:9621–9627.
13. Ji S, Jiang T, Xu K, Li S. FTIR study of the adsorption of water on ultradispersed diamond powder surface. *App Surface Science*. 1998;133:231–238.
14. Osawa E. Monodisperse single nanodiamond particulates. *Pure Appl Chem*. 2008;80:1365–1379.
15. Mitev DP, Townsend AT, Paull B, Nesterenko PN. Screening of elemental impurities in commercial detonation nanodiamond using sector field inductively coupled plasma-mass spectrometry. *J Mater Sci*. 2014;49:3573–3591.
16. Petrov P, Detkov J, Walch O, Shenderova O. Polydispersed detonation nanodiamond and approaches for its fractioning. *Proceedings of the NSTI-Nanotech 2006*; 2006 May 7–11; Boston, MA. 2006;1:150–153. nsti.org, ISBN 0-9767985-6-5.
17. Shenderova OA, McGuire GE. Science and engineering of nanodiamond particle surfaces for biological applications (review). *Biointerphases*. 2015;10:030802.
18. Krüger A; Kataoka F, Ozawa M, Fujino T, Suzuki Y, Aleksenskii AE, Ya A, Vul A, Ōsawa E. Unusually tight aggregation in detonation nanodiamond: identification and disintegration. *Carbon*. 2005;43:1722–1730.
19. Moore M. Imaging diamond with X-rays. *J Phys D: Condens Matter*. 2009;21:364217.
20. Beaucage G, Kammler HK, Pratsinis SE. Particle size distributions from small-angle scattering using global scattering functions. *Journal of Applied Crystallography*. 2004;37(4):523–535.
21. Schaefer DW, Justice RS. How nano are nanocomposites? *Macromolecules*. 2007;40:8501–8517.
22. Kane MC, Londono JD, Beyer FL, Brennan AB. Chracterization of the hierarchical structures of a dry nanopowder in a polymer matrix by X-ray scattering techniques. *J Appl Cryst*. 2009;42:925–931.
23. Glatter O, Kratky O. *Small angle X-ray scattering*. New York (NY): Academic Press; 1982.

24. Koberstein JT, Morra B, Stein RS. The determination of diffuse-boundary thickness of polymers by small-angle X-ray scattering. *J Appl Cryst.* 1980;13:34–45.
25. Schmidt PW, Avnir D, Levy D, Höhr A, Steiner M, Röhl A. Small angle X-ray scattering from the surfaces of reversed-phase silicas: power-law scattering exponents of magnitudes greater than 4. *J Chem Phys.* 1991;94:1474–1479.
26. Tomchuk OV, Bulavin LA, Aksenov VL, Garamus VM, Ivankov OI, Vul AY, Dideikin AT, Avdeev MV. Small-angle scattering from polydisperse particles with a diffusive surface. *J Appl Cryst.* 2014;47:642–653.
27. Mykhaylyk OO, Solonin YM, Batchelder DN. Transformation of nanodiamond into carbon onions: a comparative study by high-resolution transmission electron microscopy, electron energy-loss spectroscopy, X-ray diffraction, small angle x-ray scattering and ultraviolet Raman spectroscopy. *J Appl Phys.* 2005;97(7):074302.
28. Kusz J, Böhm H. Performance of a confocal multilayer x-ray optic. *J Appl Cryst.* 2002;35:8–12.
29. Ilavsky J, Jemian PR. Irena: tool suite for modeling and analysis of small-angle scattering. *J Appl Cryst.* 2009;42:347–353.
30. Ilavsky J. Nika: software for two-dimensional data reduction. *J Appl Cryst.* 2012;45:324–328.
31. Koppel DE. Analysis of macromolecular polydispersity in intensity correlation spectroscopy: the method of cumulants. *J Chem Phys.* 1972;57:4814–4820.
32. Mitchell DRG. DiffTools script package for digital micrograph. www.dmscripting.com/difftools.html.
33. Baidakova MV, Siklitsky VI, Vul AY. Ultradisperse-diamond nanoclusters. Fractal structure and diamond-graphite phase transition. *Chaos, Solitons & Fractals.* 1999;10(12):2153–2163.
34. Ozawa M, Inaguma M, Takahashi M, Kataoka F, Kruger A. Preparation and behavior of brownish, clear nanodiamond colloids. *Adv Mater.* 2007;19:1201–1206.
35. Pichot V, Comet M, Risse B, Spitzer D. Detonation of nanosized explosive: new mechanistic model for nanodiamond formation. *Diam Relat Mater.* 2015;54:59–63.

36. Vander Wal RL, Ticich TM, West JR, Householder PA. Trace metal detection by laser-induced breakdown spectroscopy. *Appl Spectrosc.* 1999;53(10):1226–1236.
37. Cremers DA, Radziemski LJ. *Handbook of laser-induced breakdown spectroscopy.* Chichester (UK): John Wiley & Sons; 2013.
38. Gibson N, Shenderova O, Luo TJM, Moseenkov S, Bondar V, Puzyr A, Purtov K, Fitzgerald Z, Brenner DW. Colloidal stability of modified nanodiamond particles. *Diam Relat Mater.* 2009;18:620–626.
39. Krüger A, Kataoka F, Ozawa M, Fujino T, Suzuki Y, Aleksenskii AE, Vul AY, Ōsawa E. Unusually tight aggregation in detonation nanodiamond: identification and disintegration. *Carbon.* 2005;43:1722–1730.
40. Zhang X, Fu C, Feng L, Ji Y, Tao L, Li QHS, Wei Y. PEGylation and polyPEGylation of nanodiamond. *Polymer.* 2012;53(15):3178–3184.
41. Yang YD, Xu JH, Yang LM. Preparation of a nanodiamond colloid from nanodiamond powder resulting from explosive detonation. *New Carbon Materials.* 2015;30(2):181–185.
42. Motahari H, Malekfar R. Spectroscopic investigation for purity evaluation of detonation nanodiamonds: experimental approach in absorbance and scattering. *J Clust Sci.* 2017;28:1923–1935.
43. Roy RK, Deb B, Bhattacharjee B, Pal AK. Synthesis of diamond-like carbon film by novel electrodeposition route. *Thin Solid Films.* 2002;422:92–97.
44. Pang H, Wang X, Zhang G, Chen H, Guohua L, Yang S. Characterization of diamond-like carbon films by SEM, XRD and Raman spectroscopy. *Appl Surface Sci.* 2010;256:6403–6407.
45. Schaefer DW, Rieker T, Agamalian M, Lin JS, Fischer D, Sukumaran S, Chen C, Beaucage G, Herd C, Ivie J. Multilevel structure of reinforcing silica and carbon. *J of Appl Cryst.* 2000;33:587–591.
46. Marković I, Ottewill RH, Cebula DJ, Field I, Marsh JF. Small angle neutron scattering studies on non-aqueous dispersions of calcium carbonate. *Colloid and Polymer Sci.* 1984;262:648–656.
47. Barnett CE. Some applications of wave-length turbidimetry in the infrared. *J Phys Chem.* 1942;46:69–75.

48. Vul AY, Eidelman ED, Aleksenskiy AE, Shvidchenko AV, Dideikin AT, Yuferev VS, Lebedev VT, Kul'velis YV, Avdeev MV. Transition sol-gel in nanodiamond hydrosols. *Carbon*. 2017;114:242–249.
49. Osawald S, Yushin G, Mochalin V, Kucheyev SO, Gogotsi Y. Control of sp^2/sp^3 carbon ratio and surface chemistry of nanodiamond powders by selective oxidation in air. *J Am Chem Soc*. 2006;128:11635–11642.
50. Shenderova O, Koscheev A, Zaripov N, Petrov I, Skryabin Y, Detkov P, Turner S, Van Tendeloo G. Surface chemistry and properties of ozone-purified detonation nanodiamonds. *J of Phys Chem. C*. 2011;115:9827–9837.

List of Symbols, Abbreviations, and Acronyms

1-D	one-dimensional
2-D	two-dimensional
Al	aluminum
ARL	US Army Research Laboratory
BF	bright field
C	carbon
C ₁₉ H ₃	nonadecene
C ₂	diatomic carbon
C ₂₃ H ₄	tricosane
Ca	calcium
CCD	charge-coupled device
CCDC	US Army Combat Capabilities Development Command
CN	cyano radical
Co	cobalt
Cr	chromium
Cu	copper
DLS	dynamic light scattering
DND	detonation nanodiamond
EELS	electron energy loss spectroscopy
Fe	iron
FFT	fast Fourier transform
FTIR	Fourier transform infrared
GNP	graphite nanoparticle
H	hydrogen
HAADF	high-angle annular dark field
K	potassium

Li	lithium
LIBS	laser-induced breakdown spectroscopy
Mg	magnesium
Mn	manganese
N	nitrogen
Na	sodium
NaOH	sodium hydroxide
ND	nanodiamond
NIBS	noninvasive backscatter
NP	nanoparticle
O	oxygen
P	phosphorous
PDF	Powder Diffraction File
S	sulfur
SAXS	small-angle X-ray scattering
Si	silicon
SLD	scattering length density
STEM	scanning transmission electron microscopy
TEM	transmission electron microscopy
Ti	titanium
XEDS	X-ray energy-dispersive spectrometry
XRD	X-ray diffraction

1 DEFENSE TECHNICAL
(PDF) INFORMATION CTR
DTIC OCA

1 CCDC ARL
(PDF) FCDD RLD CL
TECH LIB

8 CCDC ARL
(PDF) FCDD RLW LB
C-C WU
J L GOTTFRIED
R PESCE-RODRIGUEZ
N TRIVEDI
FCDD RLW MC
S WALCK
FCDD RLW ME
A DIGIOVANNI
M IVILL
FCDD RLW MG
F BEYER

2 TEXAS TECH UNIVERSITY
(PDF) K MILLER
M PANTOYA